

Morphology and Charge Transport in P3HT: A Theorist's Perspective

Carl Poelking, Kostas Daoulas, Alessandro Troisi, and Denis Andrienko

Abstract Poly(3-hexylthiophene) (P3HT) is the fruit fly among polymeric organic semiconductors. It has complex self-assembling and electronic properties and yet lacks the synthetic challenges that characterize advanced donor–acceptor-type polymers. P3HT can be used both in solar cells and in field-effect transistors. Its morphological, conductive, and optical properties have been characterized in detail using virtually any and every experimental technique available, whereas the contributions of theory and simulation to a rationalization of these properties have so far been modest. The purpose of this review is to take a snapshot of these results and, more importantly, outline directions that still require substantial method development.

Keywords Charge transport · Conjugated polymers · Morphology · Organic semiconductors · P3HT · Simulation

Contents

- 1 Introduction
- 2 Morphology
 - 2.1 Single Molecules
 - 2.2 Crystalline Oligothiophenes
 - 2.3 Amorphous Melts and Blends

C. Poelking and D. Andrienko (✉)
Max Planck Institute for Polymer Research, Ackermannweg 10, 55128 Mainz, Germany
e-mail: carl.poelking@mpip-mainz.mpg.de; denis.andrienko@mpip-mainz.mpg.de

K. Daoulas
Max Planck Institute for Polymer Research, Ackermannweg 10, 55128 Mainz, Germany

InnovationLab GmbH, 69115 Heidelberg, Germany
e-mail: daoulas@mpip-mainz.mpg.de

A. Troisi
Department of Chemistry and Centre for Scientific Computing, University of Warwick,
Coventry CV4 7AL, UK
e-mail: a.troisi@warwick.ac.uk

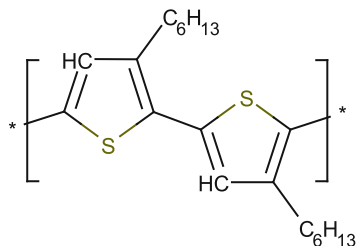
- 3 Coarse-Grained Models
 - 3.1 Structure-Based Coarse-Graining
 - 3.2 Soft Models
- 4 Rate-Based Description of Charge Transport
 - 4.1 Rates
 - 4.2 Reorganization Energy
 - 4.3 Electronic Coupling Elements
 - 4.4 Site Energies
 - 4.5 Charge Mobility
 - 4.6 Autocorrelation of Electronic Couplings and Site Energies
- 5 First-Principles-Based Calculations for Large Models of Polymer
 - 5.1 The Charge Localization–Length Problem
 - 5.2 Strategies for Large-Scale Electronic-Structure Calculations of Polymer Models
 - 5.3 Results from the Computation of the Wavefunction for Large-Scale Polymer Models
- 6 Outlook
- References

1 Introduction

Thiophene-based conjugated polymers have accompanied, if not originated, the interest in conductive polymer materials and their application in organic field-effect transistors (OFETs) and organic photovoltaic (OPV) devices [1]. The most studied representative of this class of materials is poly(3-hexyl-thiophene) (P3HT) with its regioregular (head-to-tail) isomer (see Fig. 1), as first synthesized by Rick McCullough in 1992 [2]. Polythiophenes, however, were already an intensely studied class of conjugated polymers, a rudimentary description of the compound being published as early as 1883 [3]. The first polymerization reactions with high yield and small concentrations of synthesis impurities were reported in 1980 [4, 5]. These compounds were essentially not processable due to the strong interaction of the conjugated backbones. In 1986, Elsenbaumer reported the synthesis of easily processable poly(alkyl-thiophenes) (PATs) [6]. Solution-processed into thin films, these materials could exhibit reasonable conductivities limited, however, by the disorder that results from a regiorandom attachment of the side chains to the thiophene monomers. It was the synthesis of regioregular (rr) P3ATs [2] that eventually paved the way for applications in devices such as OFETs and OPV cells. Here, we recapitulate key experimental results relevant to polymorphism, formation of self-assembled nanostructures, and charge transport in rr-P3HT. An extended overview is provided in the rest of the contributions of this volume, various books, and monographs (e.g., [7])

Like many conjugated polymers, P3HT is a polymorph, i.e., forms different crystal structures depending on processing conditions. The most frequently observed are so-called forms I and II [8], which differ by the side chain conformation and interdigitation, inclination of conjugated backbones with respect to the stacking direction, and the shift of successive (along the π -stacking direction) polymer chains [9]. Form I, which is observed after annealing, is the structure encountered in most studies dealing with OFETs and OPVs. It has a monoclinic

Fig. 1 Regioregular poly (3-alkyl-thiophene) (P3HT)



unit-cell (for bulk P3HT samples X-ray diffraction, XRD, provides $a = 1.60$ nm, $b = 0.78$ nm, and $c = 0.78$ nm [10]). Polymorph II has been found to have a significantly smaller unit cell dimension along the a -axis and has thus been assumed to have interdigitated alkyl groups [8], which distinguishes it from form I. Upon heating, form II irreversibly transforms into form I. This phase transition is accompanied by a change in unit-cell dimensions, with interlayer spacings increasing and intrastack distances decreasing. A similar first-order phase transition has been described recently in a combined infrared-spectroscopy and wide-angle XRD study for a non-interdigitated metastable polymorph that transforms into the stable form I, hence establishing a third polymorph, I' [11, 12]. Simulated unit cells of polymorphs I and I' are shown in Fig. 2.

On a mesoscale, crystallization from supercooled solutions in poor solvents can lead to the formation of secondary structures, notably nanofibers, with a width of tens of nanometers and length of several micrometers [14].

Charge transport in P3HT has been studied with the aim of relating regioregularity, molecular weight and, hence, morphology to hole mobility, and thus to the efficiency of P3HT/methanofullerene (PCBM) bulk heterojunction solar cells, for which the power conversion efficiency was reported to be 4.4% as early as 2005 [15]. Hole mobilities of 10^{-5} cm²/V s (10^{-4} cm²/V s) were measured for 94% (98%) regioregular P3HT using the time-of-flight (TOF) technique [16]. Dispersive transients of the regiorandom P3HT indicated that the polymer is conductive, yet its mobility could not be extracted from TOF measurements due to sizeable disorder. The mobility temperature dependence, analyzed using the Gaussian disorder model (GDM), suggested an energetic disorder of around 50–60 meV. Both hole and electron TOF mobilities were reported to be independent of the molecular weight up to 20 kDa, and then decreased by an order of magnitude as molecular weight increased to 120 kDa [17]. The reported zero-field mobilities for shorter chains were of the order of 10^{-4} cm²/V s. A GDM-fitted energetic disorder of 71(54) meV was extracted for short (long) chains.

Meanwhile, field-effect mobilities ranging around $\mu \sim 10^{-5}$ cm²/V s were reported for the very first OFET device that used polythiophene for the semiconducting channel [18]. By choosing rr-P3HT, μ could be increased by three orders of magnitude [19]. OFET mobilities of ~ 0.1 cm²/V s were measured as a function of the molecular weight after spin-casting from higher boiling point solvents [20]. The field-effect mobility was found to increase with molecular weight in spite of reduced crystallinity. This was attributed to either better interconnectivity of the

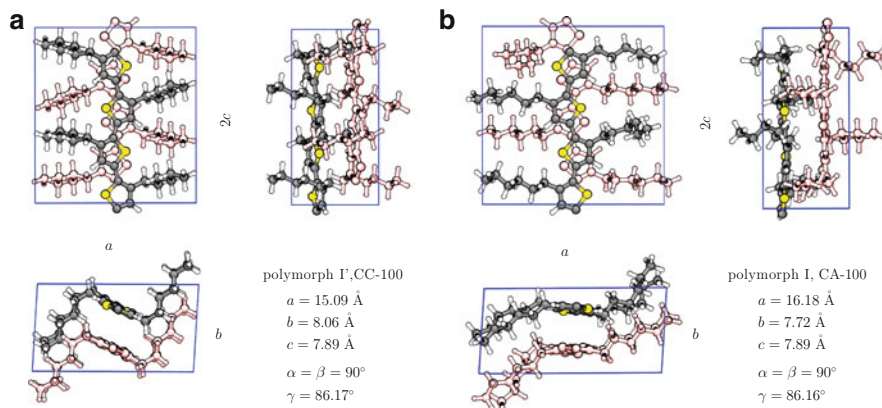


Fig. 2 Unit cells of polymorphs I' (a) and I (b) as obtained from molecular dynamics simulations. To highlight the backbone and side chain packing, we use C for crystalline and A for amorphous states, i.e., CA-100 corresponds to a system with a crystalline arrangement of backbones, amorphous packing of side-chains, and regioregularity of 100%. CC-100 corresponds to a system with crystalline side chains and 100% regioregularity. Adapted with permission from Poelking et al. [13]. Copyright (2013) American Chemical Society

polymer network [21] or smaller intrachain ring torsions present in high molecular weight molecules [22].

Transistor hole mobilities have even been reported for individual P3HT nanofibers [14, 23, 24]. Along the fiber, this mobility was as high as $0.06 \text{ cm}^2/\text{V s}$. An energetic disorder of 108 meV was extracted from temperature-dependent measurements.

Stimulated by this multitude of experimental investigations, a number of theoretical studies have been conducted to rationalize the wide spectrum of mobilities obtained for a single compound and link the transport characteristics to the self-assembly properties, morphology, and electronic structure of P3HT. The controversy started when examining conformations of a single isolated chain: the thiophene dimer was reported to adopt a twisted backbone conformation [25], whereas increasing the oligomer length resulted in a planarized backbone. The situation with oligomer assemblies is even more involved; indeed, we still do not know the order of crystalline polymorphs on the energy axis, cannot quantify the density of defects in a crystalline morphology, or quantify the relative volume fractions of crystalline and amorphous phases. We do not really understand what exactly limits charge transport in ordered lamellar systems: is it large energetic disorder or small electronic couplings? Why is the hole transport strongly dispersive even though the reported energetic disorder is moderate? How does regioregularity contribute to morphological ordering, density of states, and electronic couplings? In which ways does molecular weight impact mobility? Our goal is to summarize approaches and answers to some of these questions from a theoretical perspective and to provide an outlook for the remaining questions.

2 Morphology

The theoretical and computational toolbox used to study self-assembling properties of conjugated polymers is very versatile: On the highest level of resolution, it includes accurate quantum chemical calculations capable of predicting the properties of isolated oligomers and dimers, normally without side chains. Less computationally demanding density functional methods can deal with much longer oligomers (10–20 repeat units), including side chains, and are often used to compare ground state energies of experimentally proposed arrangements of atoms in a unit cell. To assess crystalline packing modes at ambient conditions and during annealing, as well as to study amorphous melts and longer chain lengths, classical force fields have been parametrized. To access even longer length and time scales (micrometers, microseconds), coarse-grained models have been developed to study amorphous melts and liquid-crystalline phases of P3HT.

The ultimate goal of these simulations is to self-assemble the polymer *in silico*, i.e., to predict its polymorphs as well as the degree of disorder in the kinetically trapped molecular arrangements. The honest assessment is that we are fairly far from achieving this goal. The main obstacles are insufficient accuracy of methods at a specific level of resolution, long simulation times required to study self-assembly, and uncontrolled error propagation from one level to another, e.g., when parametrizing force fields based on quantum chemical calculations, or developing coarse-grained models using force-field-generated reference data.

We will provide a summary of simulation results, starting with single-molecule properties and then expanding to molecular arrangements of P3HT in crystals, melts, and finally binary mixtures with PCBM, a typical acceptor used in organic solar cells.

2.1 *Single Molecules*

Ab initio methods have been extensively used to analyze conformations of the conjugated backbone and side-chain orientations with respect to the plane of conjugation [25]. Here, the extended π -conjugated system flattens the backbone, whereas nonbonded interactions between consecutive repeat units (i.e., steric repulsions between hydrogen atoms, Coulomb interactions, and van der Waals interactions) often tend to distort its planarity. For P3HT, both planar [26] and nonplanar stable geometries have been reported, depending on the side-chain orientation [27]. At the B3LYP/6-31+G level of density functional theory (DFT), the nonplanar backbone has an energy of ~ 0.03 eV lower (per monomer) than the planar backbone (evaluated in a 10-mer) [28]. This indicates that chain conformations in the bulk are predominantly determined by interchain van der Waals and Coulomb interactions, a conclusion also drawn from calculations of molecular dimers [29].

Because typical energy differences between planar and nonplanar conformations are in the order of tens of millielectronvolts, which is the accuracy threshold of density functional methods, one is forced to use more accurate (and computationally demanding) quantum-chemical methods. However, the ground-state twist angle between repeat units has been found to depend on the oligomer length, saturating at about ten repeat units. Furthermore, torsional potentials are correlated up to the second-nearest-neighbor rings [30], thus making geometry predictions a formidable task even for isolated oligomers [31].

2.2 Crystalline Oligothiophenes

Both density functional and force-field calculations have been used to study crystalline P3HT mesophases. Density functional calculations have been primarily used to establish whether experimentally reported crystal structures correspond to well-defined energy minima [32–35]. Using a van-der-Waals-corrected generalized gradient approximation (GGA) functional, Dag and Wang concluded that the crystal with shifted backbones (i.e., with one of the thiophene layers shifted along the chain direction by the thiophene–thiophene distance) and side chains rotated around the torsion angle is the most stable of three studied structures [36]. Xie et al. reached the conclusion that a structural motif without this registry shift and without rotation of the side chains, but instead with a small backbone tilt, has the lowest potential energy [34]. Similar to the situation with a single isolated chain, typical energy differences between different packing motives are in the order of 10 meV per unit cell and, hence, theoretical methods are at their accuracy limits, making it difficult to rank different molecular arrangements. Also, unit-cell optimizations are performed at zero Kelvin, meaning that entropic effects, notably the chain excluded volume, are ignored.

To study larger systems and longer timescales, various flavors of P3HT force fields were developed. In the majority of cases, parameters of an existing force field were refined in order to reproduce the torsional potential between thiophene units and electrostatic potential around an isolated oligomer [13, 37]. The parametrization has been subsequently refined to account for the change in the backbone potential with oligomer length [13, 26, 28, 38–40]. To this end, atomistic simulations have been used to analyze proposed packing arrangements of three P3HT polymorphs (phases I, I', and II; see Fig. 2), and to scrutinize the effect of regioregularity on paracrystalline, dynamic, and static nematic order parameters [13]. Molecular dynamics simulations suggest that the most stable P3HT polymorph has planar thiophene backbones shifted by one thiophene ring with respect to each other. Hexyl side chains are twisted away from the backbone in a *trans* fashion, resulting in a non-interdigitated packing structure, although stable structures with interdigitated side chains were also reported [41]. Force-field-based estimates of the mass density (1.05 g cm^{-3}), melting temperature (490 K), and surface tension (32 mN/m) all agree with the reported experimental values

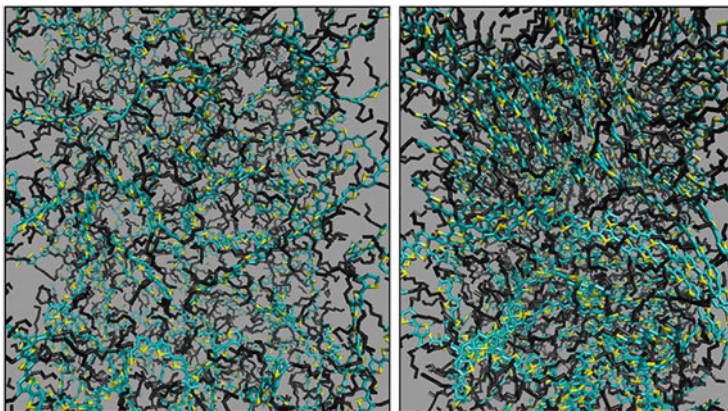


Fig. 3 Typical configuration of the amorphous system after annealing the crystal at high temperatures (*left*). Onset of crystallization at 300 K acquired at the end of the gradual cooling process that was started from the amorphous melt (*right*). Adapted with permission from Alexiadis and Mavrantzas [42]. Copyright (2013) American Chemical Society

[40]. One should note that even on this classical level of description, only highly crystalline morphologies and high-temperature amorphous melts can be studied. Still, some indications of local-chain ordering upon cooling of amorphous high-temperature melts (see Fig. 3) have been observed [42].

2.3 Amorphous Melts and Blends

Early simulations of amorphous systems considered thiophene oligomers as a model for P3HT. Alignment of polymer chains and thiophene units within chains have for instance been studied in a Monte-Carlo approach [43]. The authors were able to reproduce the density of the amorphous mesophase (an estimate of 1.06 g cm^{-3} was given) and concluded that chains tend to align parallel to each other, while thiophene rings of neighboring chains tend to adopt parallel or anti-parallel π -stacked arrangements. Systems with much shorter chains had significantly denser packing (predicted density 1.4 g cm^{-3}) and stronger alignment, a result obtained using molecular dynamics simulations [44].

Amorphous melts of oligomers of P3HT were also simulated in order to calculate the glass transition temperature (300 K) and, hence, validate the atomistic force field [40] and to develop coarse-grained models of P3HT in a liquid state approaching 500–600 K [45, 46]. Simulations of free-standing films of P3HT melts have been used to estimate the room-temperature value of surface tension ($21\text{--}36 \text{ mN m}^{-1}$) [47]. Amorphous melts of P3HT are, however, of only moderate interest because the conductive abilities of this polymer are related to its high degree of lamellar ordering.

In order to understand molecular ordering and electronic processes in bulk heterojunction devices, blends of P3HT oligomers with fullerene and PCBM have been simulated at different levels of resolution. Atomistic simulations showed that bulk oligothiophenes (five chains of 20 repeat units each) tend to cluster better than oligothiophene/fullerene systems [48]. Prototypical model interfaces have been used to evaluate energetic profiles for electrons and holes [49]. Coarse-grained simulations could observe the onset of phase separation [45], distributions of domain sizes, and interface-to-volume ratios [50] in P3HT/PCBM mixtures. Nevertheless, the field of coarse-grained modeling of conjugated polymers is still in its infancy. Complications reside in the large persistence length and anisotropic nonbonded interactions that promote π - π stacking. We will discuss various strategies for developing coarse-grained models of conjugated polymers in Sect. 3.

3 Coarse-Grained Models

Apart from the local molecular packing discussed so far, mesoscopic ordering of conjugated polymers is equally important for the functionality of organic semiconducting devices. In a bulk heterojunction solar cell, for example, domain sizes of the donor and acceptor mesophases have considerable impact on cell efficiency. To predict and analyze such effects, modeling strategies that target the morphology on length scales reaching several hundreds of nanometers, the typical thickness of the active layer in a polymer-based solar cell, are required. With the currently available computational power, such system sizes can only be addressed on a coarse-grained level.

The idea of coarse-graining relies on the separation of time and length scales. For many polymeric systems, especially polymer melts, the chemical details, although strongly affecting material behavior on the microscopic level, become less important on the mesoscale, where simplified representations of polymer architecture and interactions can be used. In conjugated polymers, however, the mesoscale features of the morphology couple across many length scales: π - π stacking for instance promotes the formation of lamellae, which in turn self-assemble into supramolecular structures. Predicting this hierarchical self-assembly is the main target (and challenge) of coarse-grained modeling of conjugated polymers.

Coarse-graining strategies can be subdivided into bottom-up and top-down approaches [51, 52]. In bottom-up coarse-graining, the model is constructed to reproduce physical quantities known from a more detailed description of the system [53]. In other words, a fine-grained representation of the system is projected onto a representation with fewer degrees of freedom. This projection is not unique, and various techniques have been suggested, including structure-based coarse-graining [53, 54], force-matching [55, 56], and relative entropy frameworks [57]. Top-down

approaches, on the contrary, derive the coarse-grained model from macroscopic observables (e.g., the phase behavior). These are often based on experimental measurements [51, 52, 58] but can also incorporate elements of bottom-up coarse-graining. In the following sections, we review the results obtained using structure-based coarse-grained models and also introduce a coarse-graining technique based on soft interaction potentials.

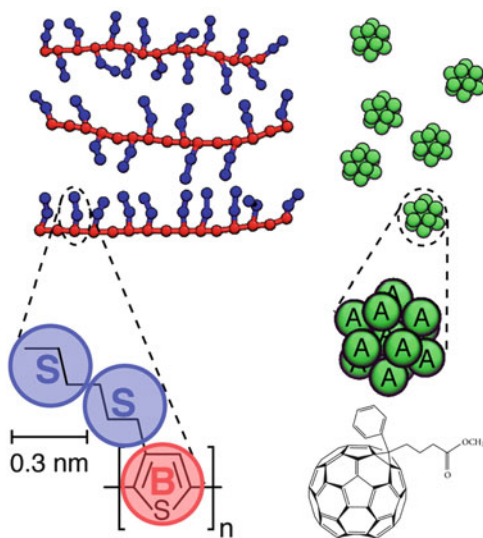
3.1 Structure-Based Coarse-Graining

The idea of structure-based coarse-graining is to match structural properties, such as radial distribution functions, of the fine- and coarse-grained systems. Structure-based coarse-grained models have been developed for melts [45, 46], high-temperature (liquid) mixtures of P3HT/PCBM [45, 50, 59], and solutions of P3HT [60]. The P3HT monomers are normally coarse-grained into three interaction sites placed at the center of mass of the thiophene rings, then on the first and last three methyl groups of the hexyl side-chain, as shown in Fig. 4. The bonded and nonbonded interaction parameters are optimized using the iterative Boltzmann inversion method [54, 61], although phenomenological refinement is also used [59].

The three-site models allow for self-assembling polymer backbones into lamellar arrangements [59, 60]. They have also been used to study the morphology of phase-separated P3HT/PCBM blends, where explicit incorporation of side chains helped to understand penetration of acceptor molecules into side chains as a function of their grafting density along the backbone. No intercalation was found for P3HT, in contrast to poly(bithiophene-alt-thienothiophene) (PBTTT), which has a lower grafting density of side chains [59]. A further advantage of coarse-graining is that solvent-mediated interactions can be incorporated into coarse-grained interactions, leading to a dramatic decrease in the number of degrees of freedom. Simulations of P3HT aggregation in solutions with anisole could reproduce the experimentally observed aggregation of P3HT as a function of temperature with the back-folded hairpins of stacked P3HT molecules [60]. The spacing between P3HT lamellae was found to be 1.7 nm, which is comparable to experimental observations [9].

Three-site coarse-grained models normally employ orientationally *isotropic* nonbonded interactions and are parametrized either on high-temperature P3HT melts or solutions. Thus, by construction, they cannot capture the directionality of π - π interactions between thiophenes. The backbones of the P3HT chains within the same lamella are also less correlated, leading to smectic-like ordering [59, 60]. In fact, this type of ordering has been reported experimentally, although in a narrow temperature window, prior to melting [10].

Fig. 4 *Left:* Three-site coarse-grained model of polythiophene derivatives with different side chain grafting densities. *Right:* PCBM modeled by a collection of 13 coarse-grained beads. Bead types are labeled by letters A (buckyball), B (backbone), and S (side chain). Adapted with permission from Jankowski et al. [59]. Copyright (2013) American Chemical Society



3.2 Soft Models

The three-site models with explicit beads for side chains are too complex for simulations of dense systems and long chains. For homopolymer melts, oligomers of 15 repeat units have been used [59], whereas simulations of P3HT/PCBM blends employed chains of 48 repeat units [45]. Further reducing the number of degrees of freedom, e.g., by removing coarse-grained side chains, necessitates orientationally anisotropic interaction potentials, otherwise even the lamellar order is no longer produced. In other words, anisotropic interactions are needed to account for the conformational frustration of side chains and the energetically favorable stacking of backbones. In this sense, they incorporate entropic and enthalpic contributions to the free energy of the system.

As the model becomes cruder and cruder, the number of microscopic states that correspond to the same coarse-grained state increases. As a result, the coarse-grained interaction potentials become softer. This, in combination with the reduction in the degrees of freedom, boosts computational efficiency. At the same time, the thermodynamic nature of the coarse-grained potentials becomes more prominent and transferability is gradually lost [62]. To remedy the situation, thermodynamic properties of the system can be incorporated into the coarse-grained model by using (phenomenological) top-down approaches. For conjugated polymers, the symmetry of the mesophase can be directly included into the anisotropic interaction potential, as has been shown for liquid crystalline mesophases [63, 64] observed experimentally in poly[3-(2'-ethyl)hexylthiophene] and poly(3-dodecylthiophene) [65, 66].

In such coarse-grained models, nonbonded interactions are chosen such that the system possesses a desired phase behavior, e.g., a nematic to isotropic transition. In practice, one starts with an appropriate density functional, in the spirit of

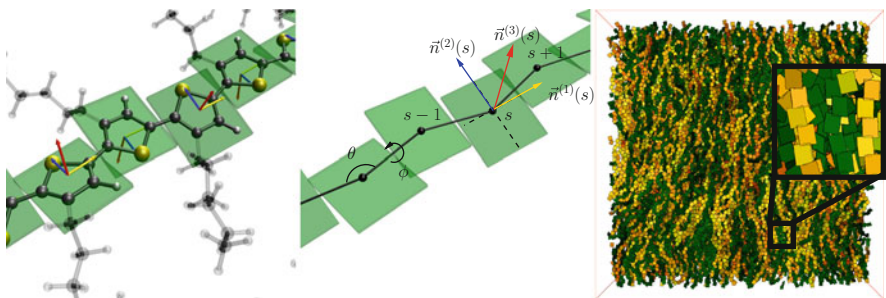


Fig. 5 Atomistic and coarse-grained representation of a P3HT chain (*left*), including coarse-grained angular (θ) and dihedral (ϕ) degrees of freedom (*center*). Biaxial nematic alignment in a melt of P3HT chains (*right*). Adapted with permission from Gemünden et al. [64]. Copyright (2013) American Chemical Society

field-theoretical descriptions of polymeric liquid crystals [67–71]. Each s -th coarse-grained thiophene of the i -th molecule with coordinate $\mathbf{r}_i(s)$ is assigned an orthonormal set of vectors $\{\mathbf{n}_i^{(1)}(s), \mathbf{n}_i^{(2)}(s), \mathbf{n}_i^{(3)}(s)\}$ as illustrated in Fig. 5. A repeat unit is smeared into a density distribution $\omega(\mathbf{r} - \mathbf{r}_i(s))$, which allows for collective degrees of freedom:

$$\begin{aligned} \hat{\rho}(\mathbf{r}) &= \sum_{i=1}^n \sum_{s=1}^N \omega(\mathbf{r} - \mathbf{r}_i(s)) \\ \hat{Q}_{\alpha\beta}(\mathbf{r}) &= \rho_0^{-1} \sum_{i=1}^n \sum_{s=1}^N \omega(\mathbf{r} - \mathbf{r}_i(s)) q_{i,\alpha\beta}(s) \\ \hat{B}_{\alpha\beta}(\mathbf{r}) &= \rho_0^{-1} \sum_{i=1}^n \sum_{s=1}^N \omega(\mathbf{r} - \mathbf{r}_i(s)) b_{i,\alpha\beta}(s) \end{aligned} \quad (1)$$

where $\alpha, \beta = x, y, z$, and

$$q_{i,\alpha\beta}(s) = \left[\frac{3}{2} n_{i,\alpha}^{(1)}(s) n_{i,\beta}^{(1)}(s) - \frac{\delta_{\alpha\beta}}{2} \right] \quad (2)$$

$$b_{i,\alpha\beta}(s) = \left[n_{i,\alpha}^{(2)}(s) n_{i,\beta}^{(2)}(s) - n_{i,\alpha}^{(3)}(s) n_{i,\beta}^{(3)}(s) \right] \quad (3)$$

are the orientational order parameters. The density cloud $\omega(\mathbf{r} - \mathbf{r}_i(s))$ represents, to some extent, the distribution of the underlying microscopic degrees of freedom [72]. Because molecules in a nematic phase are orientationally ordered but positionally disordered and side chain conformations strongly fluctuate, the average spatial distribution of monomers can be approximated by a spherical uniform density cloud, $\omega(\mathbf{r}) = \frac{3}{4\pi\sigma^3}$ if $r \leq \sigma$, zero otherwise. For P3HT, for example, $\sigma = 0.6$ nm, which is close to the length of a hexyl chain in the all-*trans* configuration, ~ 0.76 nm.

The nonbonded interactions are then defined through a free-energy functional of the collective variables [64]:

$$\begin{aligned}
 H_{\text{nb}} \left[\hat{\rho}, \hat{\mathbf{Q}}, \hat{\mathbf{B}} \right] = & \int d\mathbf{r} \frac{\hat{\kappa} \rho_0}{2} \left(\frac{\hat{\rho}(\mathbf{r})}{\rho_0} - 1 \right)^2 \\
 & - \frac{\hat{\nu} \rho_0}{3} \int d\mathbf{r} \hat{\mathbf{Q}}(\mathbf{r}) : \hat{\mathbf{Q}}(\mathbf{r}) \\
 & - \frac{\hat{\mu} \rho_0}{3} \int d\mathbf{r} \{ \hat{\mathbf{Q}}(\mathbf{r}) : \hat{\mathbf{B}}(\mathbf{r}) + \hat{\mathbf{B}}(\mathbf{r}) : \hat{\mathbf{Q}}(\mathbf{r}) \} \\
 & - \frac{\hat{\lambda} \rho_0}{4} \int d\mathbf{r} \hat{\mathbf{B}}(\mathbf{r}) : \hat{\mathbf{B}}(\mathbf{r})
 \end{aligned} \tag{4}$$

Here the first term suppresses local density fluctuations [73, 74] and the rest is an analog of the Ginzburg–Landau free energy associated with the instantaneous tensorial fields $\hat{\mathbf{Q}}$ and $\hat{\mathbf{B}}$. Phenomenological parameters $\bar{\nu}$, $\bar{\mu}$ and $\bar{\lambda}$ entering this functional are normally chosen such that the thermodynamic state of interest, e.g., a biaxial–nematic mesophase, is reproduced. In this respect, mean-field estimates can help to limit the physically adequate parameter ranges. Positive isothermal compressibility, for example, requires $\bar{\kappa} > \bar{\nu} + \bar{\mu} + \bar{\lambda}$ [64].

Following similar studies with scalar collective degrees of freedom [51, 75], one can then write the effective Hamiltonian of nonbonded interactions as:

$$\begin{aligned}
 H_{\text{nb}} = & \frac{1}{2} \sum_{i,j=1s,t=1}^n \sum^N u(r_{ij}(s,t)) \left[\bar{\kappa} - \frac{2\bar{\nu}}{3} \mathbf{q}_i(s) : \mathbf{q}_j(t) - \right. \\
 & \left. - \frac{2\bar{\mu}}{3} (\mathbf{q}_i(s) : \mathbf{b}_j(t) + \mathbf{b}_i(s) : \mathbf{q}_j(t)) - \frac{\bar{\lambda}}{2} \mathbf{b}_i(s) : \mathbf{b}_j(s) \right]
 \end{aligned} \tag{5}$$

where $u(r_{ij}(s,t)) = \rho_0^{-1} \int d\mathbf{r} \omega(|\mathbf{r} - \mathbf{r}_i(s)|) \omega(|\mathbf{r} - \mathbf{r}_j(t)|)$ is the soft repulsion core expressing the overlap of the density clouds [51, 64]:

$$u(r_{ij}(s,t)) = \frac{3}{8\pi\rho_0\sigma^3} \left(2 + \frac{r_{ij}(s,t)}{2\sigma} \right) \left(1 - \frac{r_{ij}(s,t)}{2\sigma} \right)^2 \tag{6}$$

Thus, the free-energy functional is transformed into a sum over pairwise, orientation-dependent interactions. Note that bonded interaction potentials are taken into account separately and can be parametrized using atomistic simulations of a single isolated chain in θ -solvent conditions. Here bond lengths are kept fixed and harmonic angular and Ryckaert–Bellemans torsion potentials are used to reproduce the corresponding distributions [64].

Once the Hamiltonian is fully parametrized, standard sampling techniques (e.g. Monte Carlo, molecular dynamics, or dissipative particle dynamics) can be used to explore the phase space and to evaluate macroscopic observables. Note that the coarse-grained hexylthiophenes interact even at a distance of $2\sigma = 1.2$ nm, which is almost twice the average separation of their centers of mass, estimated as $\rho_0^{-1/3} \approx 0.63$ nm. In order to obtain realistic values for the effective excluded volume, the interactions for strong overlaps of the density clouds must be weak, i.e., $\bar{\kappa}u(0) \sim k_B T$. This results in soft potentials and boosts the efficiency of phase-space sampling, especially if the Monte Carlo algorithm is used.

Simulations using the reptation algorithm [76, 77] showed that one can equilibrate systems on the scale of $\approx 50 \times 50 \times 50$ nm³, containing around 5×10^{-5} hexylthiophenes with up to 32 monomers per chain. Depending on the coupling strength $\bar{\lambda}$ and the degree of polymerization, plate-like nematic mesophases (with normals of the thiophene rings parallel to the director) as well as biaxial phases (see Fig. 5 for a representative snapshot) have been observed. It has also been shown that the model predicts reasonable values for the persistence length and Frank elastic constants [64].

With the large-scale morphology at hand, some insights can be obtained on how the collective orientation of chains affects the energetic landscape for drift-diffusing charges. This has been done by splitting polymer segments onto conjugated segments (using a simple criterion for the torsion angle [78]; see, however, Sect. 5.1) and evaluating gas-phase ionization energies of these segments. Even this crude model predicts that isotropic melts consist of short conjugated segments with defects uniformly distributed along the chains. In the biaxial nematic case, the average segment length increases significantly, and the collective orientation of these segments leads to a spatially correlated energetic landscape, even without accounting for long-range Coulomb interactions [64].

4 Rate-Based Description of Charge Transport

We will now discuss the semiconducting properties of P3HT. When choosing an appropriate model for charge transport in this polymer, we have to rely on the experimentally observed increase in mobility with increasing temperature. This is interpreted as a sign for temperature-activated hopping transport. In other words, charges (charged states) are localized and charge transfer reactions that propagate the localized states are thermally activated. Localization can occur on single molecules (typically observed in amorphous small-molecule-based organic semiconductors) or molecular assemblies (crystalline materials). In polymers, charge localizes on molecular, or conjugated, segments, as discussed in Sect. 5.1.

If charge transfer rates are known, the resulting master equation for occupation probabilities of these localized states describes charge dynamics in the system. Hence, the solution of the master equation provides information about charge

distribution, currents, and eventually mobility, all as a function of temperature, external field, charge density, and, importantly, morphology. Here we will start with the charge transfer rate and introduce microscopic quantities that affect charge dynamics.

4.1 Rates

The simplest rate expression can be derived for a system with classical harmonic vibrational degrees of freedom (semiclassical high-temperature limit) [79, 80]:

$$k_{A \rightarrow B} = \frac{2\pi}{\hbar} \frac{|J_{AB}|^2}{\sqrt{4\pi\lambda kT}} \exp\left[-\frac{(\Delta U_{AB} - \lambda)^2}{4\lambda kT}\right]. \quad (7)$$

This so-called Marcus rate depends on only three microscopic parameters: reorganization energy λ , electronic coupling J_{AB} , and driving force $\Delta U_{AB} = U_A - U_B$, all of which can be evaluated using quantum-chemical methods, classical polarizable force-fields, or quantum-classical hybrids as discussed in the following sections. Various generalizations of this expression to quantum-mechanical modes have been derived [81–84].

4.2 Reorganization Energy

The internal reorganization energy is a measure of how much the geometry of the charge transfer complex adapts as the charge is transferred. The reorganization energy can be estimated from four points on the diabatic potential energy surfaces (PES) shown in Fig. 6:

$$\begin{aligned} \lambda_{A \rightarrow B} &= U_a(\xi_A) - U_a(\xi_a) + U_B(\xi_b) - U_B(\xi_B), \\ \lambda_{B \rightarrow A} &= U_b(\xi_B) - U_b(\xi_b) + U_A(\xi_a) - U_A(\xi_A). \end{aligned} \quad (8)$$

Here, $U_{a,b}$ and $U_{A,B}$ refer to the diabatic states of molecules A and B in their neutral and charged states, respectively. Treatments that do not approximate the PES in terms of a single shared normal mode are also available [85].

An additional contribution to the overall λ results from the reorganization of the environment in which the charge transfer takes place, giving rise to λ^{out} . This outer-sphere reorganization energy contributes to the exponent in the rate expression in the same fashion as its internal counterpart. We note however that, in organic semiconductors, λ^{out} is small (~ 0.01 eV) and becomes important primarily for charge transfer in polar solvents.

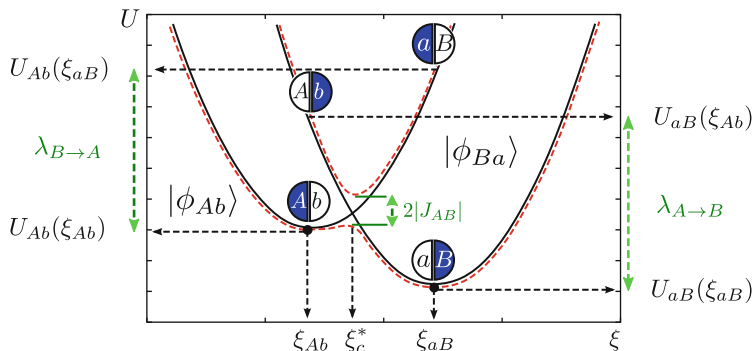


Fig. 6 Diabatic (solid black line) and adiabatic (dashed red line) potential energy surfaces of two electronic dimer states $|\phi_{Ab}\rangle$ and $|\phi_{Ba}\rangle$ participating in the charge transfer reaction along the reaction coordinate ξ . Reorganization energies $\lambda_{A \rightarrow B}$, $\lambda_{B \rightarrow A}$

For P3HT, the reorganization energy decreases to ~ 0.1 eV for a chain length of 20 monomers, which is small compared to ~ 0.2 – 0.4 eV observed in many small-molecule-based organic semiconductors due to better delocalization of the charge. Additionally, steric hindrance prevents conformational changes of the polymer chain upon charging if embedded in a π -stacked crystal. The resulting constraint on the backbone planarity helps lower the reorganization energy.

4.3 Electronic Coupling Elements

Electronic coupling elements, or transfer integrals, between molecules i and j are given by the off-diagonal matrix elements [80, 86]:

$$J_{ij} = \langle \phi_i | \hat{H} | \phi_j \rangle, \quad (9)$$

where $\phi_{i,j}$ are diabatic states, often approximated by the frontier orbitals of the molecules, and \hat{H} is the dimer Hamiltonian. These quantities are normally evaluated using electronic structure methods. Expanding the adiabatic states of the dimer in monomer states, we obtain the following secular equation:

$$(\mathbf{H} - E\mathbf{S})\mathbf{C} = 0, \quad (10)$$

where \mathbf{H} and \mathbf{S} are the Hamiltonian and overlap matrices of the system:

$$\mathbf{H} = \begin{pmatrix} e_i & H_{ij} \\ H_{ij}^* & e_j \end{pmatrix}, \quad \mathbf{S} = \begin{pmatrix} 1 & S_{ij} \\ S_{ij}^* & 1 \end{pmatrix} \quad (11)$$

and $e_i = \langle \phi_i | \hat{\mathbf{H}} | \phi_i \rangle$, $e_j = \langle \phi_j | \hat{\mathbf{H}} | \phi_j \rangle$, $H_{ij} = \langle \phi_i | \hat{\mathbf{H}} | \phi_j \rangle$, and $S_{ij} = \langle \phi_i | \phi_j \rangle$

In the basis of its eigenfunctions, the Hamiltonian operator is diagonal, $\langle \phi_n^D | \mathbf{H} | \phi_m^D \rangle = E_n \delta_{nm}$. Hence, Eq. (10) can be rewritten as:

$$H_{ij} = \sum_n \langle \phi_i | \phi_n^D \rangle E_n \langle \phi_n^D | \phi_j \rangle. \quad (12)$$

Expanding the monomer and dimer functions into a basis set of atom-centered orbitals, $|\phi_k\rangle = \sum_\alpha M_\alpha^{(k)} |\varphi_\alpha\rangle$, $|\phi_n^D\rangle = \sum_\alpha D_\alpha^{(n)} |\varphi_\alpha\rangle$, the projections read:

$$\langle \phi_k | \phi_n^D \rangle = \sum_\alpha M_\alpha^{(k)} \langle \alpha | \sum_\beta D_\beta^{(n)} | \beta \rangle = \overline{\mathbf{M}}_{(k)}^\dagger \mathbf{S} \overline{\mathbf{D}}_{(n)} \quad (13)$$

where \mathbf{S} is the overlap matrix of the atomic basis functions. The Hamiltonian and overlap then take the form:

$$H_{ij} = \overline{\mathbf{M}}_{(i)}^\dagger \mathbf{S} \mathbf{D} \mathbf{E} \mathbf{D}^\dagger \mathbf{S}^\dagger \overline{\mathbf{M}}_{(j)} \quad (14)$$

$$S_{ij} = \overline{\mathbf{M}}_{(i)}^\dagger \mathbf{S} \mathbf{D} \mathbf{D}^\dagger \mathbf{S}^\dagger \overline{\mathbf{M}}_{(j)} \quad (15)$$

The final required transformation is the diagonalization of the diabatic states imposed by the charge-transfer Hamiltonian [87]. An orthonormal basis set that retains the local character of the monomer orbitals can be obtained by using the Lödwin transformation, $\mathbf{H}^{\text{eff}} = \mathbf{S}^{-1/2} \mathbf{H} \mathbf{S}^{-1/2}$, yielding an effective Hamiltonian with entries directly related to site energies ε_i and transfer integrals J_{ij} :

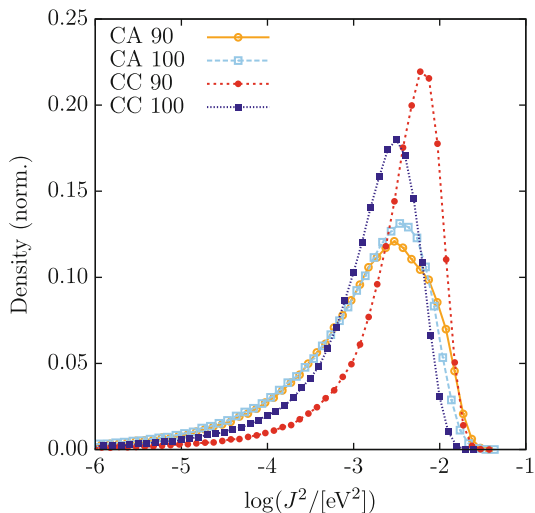
$$\mathbf{H}^{\text{eff}} = \begin{pmatrix} \varepsilon_i & J_{ij} \\ J_{ij}^* & \varepsilon_j \end{pmatrix}. \quad (16)$$

The projection method can be significantly simplified if semi-empirical methods are used for the dimer Hamiltonian [88–90] and made computationally more efficient by avoiding self-consistent dimer calculations [91].

4.3.1 Crystalline P3HT Couplings

As an illustration, we review the distribution of electronic couplings in P3HT crystals, molecular-dynamics snapshots of which are shown in Fig. 2. The diabatic states are constructed from the highest occupied molecular orbital of an optimized (B3LYP functional, 6-311 g(d,p) basis set) P3HT 20-mer. We account for the variation in dihedral angles along the polymer backbone by rotating the orbitals

Fig. 7 Distributions of squared electronic couplings for CC-100, CA-100, CC-90, and CA-90. *CA-100* corresponds to a system with a crystalline arrangement of backbones, amorphous packing of side-chains, and regioregularity of 100%. *CC-100* corresponds to a system with crystalline side chains and 100% regioregularity. Adapted with permission from Poelking et al. [13]. Copyright (2013) American Chemical Society



into the respective coordinate frames of the thiophenes. The electronic coupling elements are calculated for each molecular pair (ij) from the neighbor list using the semi-empirical ZINDO method [88–90]. A pair of molecules is added to the list of neighbors if the distance between the centers-of-mass of any of the thiophene groups is below a cut-off of 0.5 nm. This small, fragment-based cut-off ensures that only nearest neighbors are added to the neighbor list.

The distribution of electronic coupling elements is shown in Fig. 7. Note that we use CA to denote crystalline (amorphous) packing, i.e., CA-100 corresponds to a system with a crystalline arrangement of backbones, amorphous packing of side-chains, and regioregularity of 100%. Unexpectedly, the 100% regioregular P3HT with crystalline side chains (CC-100) has (on average) lower electronic couplings than the corresponding 90% regioregular phase (CC-90). This peculiar effect is most probably due to the different interlevel shift observed for the two regioregularities. Transfer integrals tend to be very sensitive to this structural mode [92]. For two perfectly aligned and optimized chains, the coupling element $|J_{ij}|^2$ can vary between 0 and 10^{-2} eV as the backbones are shifted with respect to each other along the polymer's long axis by one repeat unit, thus yielding a \sin^2 -type variation of $|J_{ij}|^2$ with interlevel shift.

Side-chain melting leads to a broadening of the distributions and a tail of very small couplings, down to 10^{-6} eV (even though only nearest neighbors are present in the neighbor list). This would obviously result in rather small average mobility values [93]. This conclusion is, however, valid only if (one-dimensional) charge-carrier transport were to occur within a static snapshot of the system; in reality, both transfer integrals and site energies are time-dependent. In order to understand whether such a static picture can be used in the case of P3HT, we compare the distributions of relaxation times of the electronic coupling elements and site energies to the distribution of escape times of a charge carrier (see Sect. 4.6).

4.4 Site Energies

The driving force, ΔU_{AB} , is given by the difference in site energy $U_A - U_B$, i.e., the energy separation between the diabatic PES minima shown in Fig. 6. U_A and U_B include both internal contributions U^{int} , i.e., the electron affinities for electrons and ionization potentials for holes of isolated molecules, and external contributions from the electrostatic (U^{est}) and induction (U^{ind}) interactions with surrounding molecules:

$$\begin{aligned}
 U_A &= U_{Ab}(\xi_{Ab}) - U_{ab}(\xi_{ab}) = \\
 &= (U_{Ab}^{\text{int}} - U_{ab}^{\text{int}}) + (U_{Ab}^{\text{est}} - U_{ab}^{\text{est}}) + (U_{Ab}^{\text{ind}} - U_{ab}^{\text{ind}}) \\
 U_B &= U_{aB}(\xi_{aB}) - U_{ab}(\xi_{ab}) = \\
 &= (U_{aB}^{\text{int}} - U_{ab}^{\text{int}}) + (U_{aB}^{\text{est}} - U_{ab}^{\text{est}}) + (U_{aB}^{\text{ind}} - U_{ab}^{\text{ind}})
 \end{aligned} \tag{17}$$

Here, the subscript ab denotes the reference (neutral) state of the system, with all molecules in their ground states.

4.4.1 Electrostatic Contribution

The electrostatic interaction energy in the site-energy calculation can be evaluated as the first-order energy correction term that results when treating an external field as a perturbing term in the molecular Hamiltonian. This term is normally evaluated using atomic distributed multipoles, where the interaction energy U_{AB} of two molecules A and B, located at positions \mathbf{X} and \mathbf{Y} reads:

$$U_{AB} = \frac{1}{4\pi\epsilon_0} \iint d^3x d^3y \frac{\rho_A(\mathbf{x})\rho_B(\mathbf{y})}{|\mathbf{Y} + \mathbf{y} - \mathbf{X} - \mathbf{x}|}. \tag{18}$$

Here ρ_A and ρ_B are the charge densities of molecules A and B, respectively.

Using the spherical-harmonic addition theorem [94], this energy can be rewritten in terms of the molecular multipole moments defined with respect to the molecule's local frame:

$$\begin{aligned}
 U_{AB} &= \frac{1}{4\pi\epsilon_0} \sum_{l_1, l_2} \sum_{k_1, k_2} \binom{l_1 + l_2}{l_1} \hat{Q}_{l_1 k_1}^A \hat{Q}_{l_2 k_2}^B \times \\
 &\quad \times S_{l_1 l_2 l_1 + l_2}^{k_1 k_2} |\mathbf{X} - \mathbf{Y}|^{-l_1 - l_2 - 1}
 \end{aligned} \tag{19}$$

These moments, $\hat{Q}_{lm}^A = \int d^3x \rho_A(x) R_{lm}(x)$, interact with each other via a tensor that contains the distance and orientation dependence. Note that here we have used $|x - y| < |\mathbf{X} - \mathbf{Y}|$ (i.e., the molecular charge densities must not interpenetrate). In this expression, the so-called S-function [95] has absorbed the orientation dependence, comprising a linear combination of products of Wigner rotation matrices and 3j-coefficients: The latter result from re-centering the spherical harmonics in the expansion around the molecular centers \mathbf{X} and \mathbf{Y} .

Due to the spherical-tensor formalism, the molecular multipole moments can be easily converted between two coordinate frames Σ_1 and Σ_2 according to $Q_{lk}^{(\Sigma_1)} = \sum_m Q_{lk}^{(\Sigma_2)} D_{mk}^l(\phi, \theta, \psi)$. Here, ϕ, θ, ψ are Euler angles and $[D_{mk}^l]$ is a Wigner rotation matrix. This conversion allows us to perform the electrostatic parametrization of a molecule within a conveniently chosen local frame, and to include the transformation from the local to the global interaction frame in a tensor that takes care of both the distance and orientation dependence:

$$T_{l_1 k_1 l_2 k_2}^{A,B} = \frac{1}{4\pi\epsilon_0} \binom{l_1 + l_2}{l_1} S_{l_1 l_2 l_1 + l_2}^{k_1 k_2} |\mathbf{X} - \mathbf{Y}|^{-l_1 - l_2 - 1} \quad (20)$$

This way, the interaction energy reduces to a compact expression, comprising only molecular multipole moments defined with respect to the molecular local frame and generic interaction tensors $T_{l_1 k_1 l_2 k_2}^{A,B}$ (tabulated up to $l_1 + l_2 = 5$ in [96]):

$$U_{AB} = \hat{Q}_{l_1 k_1}^A T_{l_1 k_1 l_2 k_2}^{A,B} \hat{Q}_{l_2 k_2}^B, \quad (21)$$

where we have used the Einstein sum convention for the multipole-moment components $l_i k_i$. The site-energy correction that enters exponentially in the Marcus rate expression for a charge localized on molecule A is then:

$$\Delta U_A^{\text{cm}} = \sum_{B \neq A} \left(\hat{Q}_{l_1 k_1}^{A,c} - \hat{Q}_{l_1 k_1}^{A,n} \right) T_{l_1 k_1 l_2 k_2}^{A,B} \hat{Q}_{l_2 k_2}^{B,n}, \quad (22)$$

where superscripts c and n denote the molecular multipole moments in the neutral and charged states, respectively, and the sum runs over all external molecules B.

4.4.2 Distributed Multipoles

In Eq. (21), we have given an expression for the electrostatic interaction energy in terms of molecule-centered multipole moments. To arrive at this expression, we required the separation between the molecular centers, $|\mathbf{X} - \mathbf{Y}|$, to be larger than the separation of any of the respective charge-carrying volume elements of the two molecules, $|x - y|$. In a molecular solid, this demand can hardly be satisfied,

considering the dense packing and (also important) strongly anisotropic charge density. This inevitably leads to breakdown of the single-point expansion at small interseparations. It is possible to avoid this breakdown by choosing multiple expansion sites (“polar sites”) per molecule in such a way as to accurately represent the molecular electrostatic potential, with a set of suitably chosen multipole moments $\{Q_{lk}^a\}$ allocated to each site. We then simply extend the expression for the interaction energy between two molecules A and B in the single-point expansion, Eq. (21), and include the sum over expansion sites $a \in A$ and $b \in B$:

$$U_{AB} = \sum_{a \in A} \sum_{b \in B} \hat{Q}_{l_1 k_1}^a T_{l_1 k_1 l_2 k_2}^{a,b} \hat{Q}_{l_2 k_2}^b \equiv \hat{Q}_{l_1 k_1}^a T_{l_1 k_1 l_2 k_2}^{a,b} \hat{Q}_{l_2 k_2}^b, \quad (23)$$

where we have used the Einstein sum convention for the site indices a and b on the right-hand side of the equation, in addition to the sum convention that is already in place for the multipole-moment components.

There are a number of strategies for arriving at such a collection of distributed multipoles [94, 97–101]. They can be classified according to whether the multipoles are derived from the electrostatic potential generated by the self-consistent field (SCF) charge density or from a decomposition of the wavefunction itself. For example, the CHELPG (charges from electrostatic potentials, grid-based) method relies on performing a least-squares fit of atom-placed charges to reproduce the electrostatic potential as evaluated from the SCF density on a regularly spaced grid [98, 102]. The distributed-multipole-analysis (DMA) approach [99, 100], developed by A. Stone, operates directly on the quantum-mechanical density matrix, expanded in terms of atom- and bond-centered Gaussian functions.

4.4.3 Induction Interaction

Similar to the distributed-multipole expansion of molecular electrostatic fields, one can derive a distributed-polarizability expansion of the molecular field response. We can start by including the multipole-expansion in the perturbing Hamiltonian term $\hat{W} = \hat{Q}_t^a \phi_t^a$, where we again use the Einstein sum convention for both superscripts a , referencing an expansion site, and subscripts t , which summarize the multipole components (l, k) in just one index. Using this approximation for the intermolecular electrostatic interaction, the second-order energy correction now reads:

$$W^{(2)} = - \sum_{n \neq 0} \frac{|\langle 0 | \hat{Q}_t^a \phi_t^a | n \rangle|^2}{W_n - W_0}. \quad (24)$$

We absorb the quantum-mechanical response into a set of intramolecular site-site polarizabilities, where $-\alpha_{tt'}^{aa'}$ yields the induced multipole moment Q_t^a at site a that results from a field component $\phi_{t'}^{a'}$ at site a' [94]:

$$\alpha_{tt'}^{aa'} \phi_{t'}^{a'} = \sum_{n \neq 0} \frac{|\langle 0 | \hat{Q}_t^a | n \rangle \langle n | \hat{Q}_{t'}^{a'} | 0 \rangle}{W_n - W_0} + h.c. \quad (25)$$

With this set of higher-order polarizabilities at hand, we obtain the induction stabilization in a distributed formulation as $W^{(2)} = -\frac{1}{2} \phi_t^a \alpha_{tt'}^{aa'} \phi_{t'}^{a'}$. The derivatives of $W^{(2)}$ with respect to the components of the field ϕ_t^a at a polar site a then yield the correction to the permanent multipole moment Q_t^a at that site: $\Delta Q_t^a = \partial W^{(2)} / \partial \phi_t^a = -\alpha_{tt'}^{aa'} \phi_{t'}^{a'}$.

Using the multipole corrections ΔQ_t^a , we can extend the electrostatic interaction energy given by Eq. (23) to include the induction contribution in the field energy U_{ext} , while accounting for the induction work U_{int} :

$$U_{\text{ext}} = \frac{1}{2} \sum_A \sum_{B \neq A} (Q_t^a + \Delta Q_t^a) T_{tu}^{ab} (Q_u^b + \Delta Q_u^b) \quad (26)$$

$$U_{\text{int}} = \frac{1}{2} \sum_A \Delta Q_t^a \eta_{tt'}^{aa'} \Delta Q_{t'}^{a'} \quad (27)$$

Here, the inverse of the positive-definite tensor $\eta_{tt'}^{aa'}$ is given simply by the distributed polarizabilities tensor $\alpha_{tt'}^{aa'}$, and we have included explicit sums over molecules A and B.

We now use a variational approach to calculate the multipole corrections ΔQ_t^a based on the total energy $\mathcal{L} = U_{\text{ext}} + U_{\text{int}}$. Variation of this function with respect to ΔQ_t^a :

$$\delta(U_{\text{ext}} + U_{\text{int}}) = \delta Q_t^a \left[\sum_{B \neq A} T_{tu}^{ab} (Q_u^b + \Delta Q_u^b) + \eta_{tt'}^{aa'} \Delta Q_{t'}^{a'} \right] \quad (28)$$

leads to a set of self-consistent equations for the induced moments, which for large systems are best solved by iteration:

$$\Delta Q_t^a = - \sum_{B \neq A} \alpha_{tt'}^{aa'} T_{t'u}^{a'b} (Q_u^b + \Delta Q_u^b). \quad (29)$$

Reinserting ΔQ_t^a into \mathcal{L} yields a total energy that can be decomposed according to three energy terms:

$$\begin{aligned}
 U_{pp} &= \sum_A \sum_{B>A} Q_t^a T_{tu}^{ab} Q_u^b \\
 U_{pu} &= \frac{1}{2} \sum_A \sum_{B>A} [\Delta Q_t^a T_{tu}^{ab} Q_u^b + \Delta Q_t^b T_{tu}^{ab} Q_u^a] \\
 U_{uu} &= 0
 \end{aligned} \tag{30}$$

Here, $U_{pp} \leftrightarrow W^{(1)}$ is the electrostatic interaction energy, i.e., the first order correction due to the interaction of permanent multipole moments. $U_{pu} \leftrightarrow W^{(2)}$ is the sought-after induction energy associated with the interaction of the induced moments on one molecule with the permanent moments on surrounding molecules. Strikingly, the interaction between induced moments on different molecules, contributing to U_{uu} , is cancelled by the induction work, as is a consequence of the self-consistent nature of the induction process, see Eq. (29).

4.4.4 The Thole Model

Equations (29) and (30) allow us to compute the electrostatic and induction energy contribution to site energies in a self-consistent manner based on a set of molecular distributed multipoles $\{Q_t^a\}$ and polarizabilities $\{\alpha_{it}^{aa'}\}$, which can be obtained from a wavefunction decomposition or fitting schemes, as discussed in Sect. 4.4.2. The $\{\alpha_{it}^{aa'}\}$ are formally given by Eq. (25). This expression is somewhat impractical (although possible, see [99]) to evaluate and various empirical methods have been developed. One of these, the Thole model [103, 104], treats polarizabilities α^a in the local dipole approximation.

The Thole model is based on a modified dipole–dipole interaction, which can be reformulated in terms of the interaction of smeared charge densities. This eliminates the divergence of the head-to-tail dipole–dipole interaction at small interseparations (Ångstrom scale) [103–105]. Smearing out the charge distribution mimics the nature of the quantum mechanical wavefunction, which effectively guards against this unphysical polarization catastrophe.

The smearing of the nuclei-centered multipole moments is obtained via a fractional charge density $\rho_f(\mathbf{u})$, which should be normalized to unity and fall off rapidly at a certain radius $\mathbf{u} = \mathbf{u}(\mathbf{R})$. This radius relates to the distance vector \mathbf{R} connecting two interacting sites via a linear scaling factor that takes into account the magnitude of the isotropic site polarizabilities α^a . This isotropic fractional charge density gives rise to a modified potential:

$$\phi(u) = -\frac{1}{4\pi\epsilon_0} \int_0^u 4\pi u' \rho(u') du' \tag{31}$$

The multipole interaction tensor $T_{ij\dots}$ (this time in Cartesian coordinates) can be related to the fractional charge density in two steps. First, it is rewritten in terms of the scaled distance vector \mathbf{u} :

$$T_{ij\dots}(\mathbf{R}) = f(\alpha^a \alpha^b) t_{ij\dots}(\mathbf{u}(\mathbf{R}, \alpha^a \alpha^b)), \quad (32)$$

where the specific form of $f(\alpha^a \alpha^b)$ results from the choice of $u(\mathbf{R}, \alpha^a \alpha^b)$. Second, the smeared interaction tensor $t_{ij\dots}$ is given by the appropriate derivative of the potential in Eq. (31):

$$t_{ij\dots}(\mathbf{u}) = -\partial_{u_i} \partial_{u_j} \dots \phi(\mathbf{u}). \quad (33)$$

It turns out that for a suitable choice of $\rho_f(\mathbf{u})$, the modified interaction tensors can be rewritten in such a way that powers n of the distance $R = |\mathbf{R}|$ are damped with a damping function $\lambda_n(\mathbf{u}(\mathbf{R}))$ [106].

There are a large number of fractional charge densities $\rho_f(\mathbf{u})$ that have been tested for the purpose of giving the best results for the molecular polarizability as well as interaction energies. For most organic molecules, a fixed set of atomic polarizabilities ($\alpha_C = 1.334$, $\alpha_H = 0.496$, $\alpha_N = 1.073$, $\alpha_O = 0.873$, $\alpha_S = 2.926 \text{ \AA}^3$) based on atomic elements yields satisfactory results [104] although reparametrizations are advised for ions and molecules with extended conjugated systems.

One of the common approaches used, e.g., in the AMOEBA force field [106], employs an exponentially decaying fractional charge density:

$$\rho(u) = \frac{3a}{4\pi} \exp(-au^3), \quad (34)$$

where $\mathbf{u}(\mathbf{R}, \alpha^a \alpha^b) = \mathbf{R}/(\alpha^a \alpha^b)^{1/6}$ and the smearing exponent $a = 0.39$. The distance at which the charge-dipole interaction is reduced by a factor γ is then given by:

$$R_\gamma = \left[\frac{1}{a} \ln \left(\frac{1}{1-\lambda} \right) \right]^{1/3} (\alpha_i \alpha_j)^{1/6}. \quad (35)$$

The interaction damping radius associated with $\gamma = 1/2$ ranges around an interaction distance of 2 \AA . A half-interaction distance on this range indicates how damping is primarily important for the intramolecular field interaction of induced dipoles.

4.4.5 Crystalline P3HT Site Energies

The expansion of the molecular field and field response in terms of distributed multipoles and polarizabilities is an efficient approach for solving for the first- and second-order corrections to the molecular Hamiltonian that result from a

perturbation by the molecular environment. Only a few studies have discussed the influence of this perturbation on the transport behavior of P3HT. Usually requiring atomistic resolution, systems of up to 10^4 thiophenes have been treated in this fashion, for example, in order to explore the density of states of P3HT in dependence on the polymorph and regioregularity or at interfaces [13, 49].

In amorphous systems, localization of charge carriers has been reported to result from fluctuations of the electrostatic potential rather than from breaks in conjugation [107]. Furthermore, an exponentially decaying tail of the density of states was found.

In crystalline systems, P3HT backbones are fully conjugated and a charge can be assumed to delocalize over an entire oligomer [108] (for a more detailed discussion see Sect. 5.1). The internal contribution to the ionization potential does not change from segment to segment and the energetic disorder is mostly due to a locally varying electrostatic potential.

The distributions in hole site energies, i.e., the differences between the energies of the system when a selected molecule is in the cationic or neutral state excluding the constant internal contribution related to the gas-phase ionization potential, are reproduced in Fig. 8 according to [13], together with the fits to a Gaussian function.

It was shown that both the width σ and the mean $\langle U \rangle$ of the distribution depend on the side-chain packing and polymer regioregularity. As expected, 100% regioregular P3HT always has narrower site energy distributions than the 90% P3HT. Interestingly, the hole becomes less stable upon side-chain melting in the 100% regioregular P3HT (the distribution shifts to more negative numbers by 0.1 eV), whereas it is stabilized by side chain melting in the 90% regioregular P3HT.

One can attribute the changes in the energetic density of states (DOS) to specific structural features [13]. The width in the distributions is governed by regioregularity, with CC-100 and CA-100 having virtually identical widths of $\sigma = 45$ and 51 meV, respectively. CC-90 and CA-90 are energetically more disordered with $\sigma = 74$ and 75 meV, respectively. The magnitude of the disorder compares well with the width of the DOS as extracted from time-of-flight experiments [16, 17], where values for σ of 56 and 71 meV, respectively, have been proposed from a fit of the field-dependence of the mobility as obtained within the Gaussian disorder model [109]. In [16], σ did not vary significantly between 94% and 98% regioregular P3HT. However, an increase in DOS width of around 30 meV can drastically impact charge mobility in the case of a one-dimensional connected hopping network, which can be assumed to appropriately reflect conditions in crystalline lamellae.

On the level of chain ordering, the increase in energetic disorder can also be related to the increase in paracrystallinity along the π -stacking direction [13]. Considering that the hole–quadrupole interactions associated with thiophene dimers are the leading contributors to site energies here, this origin for the increase in σ is fully justified and explains the similar energetic disorder computed for CC-100 and

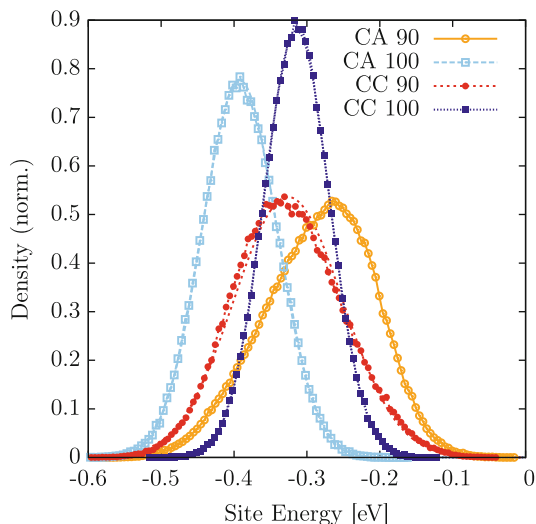


Fig. 8 Densities of state together with Gaussians fitted to CC-100, CA-100, and CC-90. Note the aberration from a Gaussian lineshape found for CA-90, which results from slipping defects in the lamellar stack. *CA-100* corresponds to a system with a crystalline arrangement of backbones, amorphous packing of side-chains, and regioregularity of 100%. *CC-100* corresponds to a system with crystalline side chains and 100% regioregularity. Adapted with permission from Poelking et al. [13]. Copyright (2013) American Chemical Society

CA-100. Notably, gliding-type paracrystallinity, measured along the c axis, does not strongly affect the electrostatic interactions between charged conjugated planes.

Shifts of the mean $\langle U \rangle$ of the site-energy distributions have been linked to the negative quadrupole moment of thiophene dimers: A hole localized on a polymer chain will be stabilized on an electrostatic level due to the quadrupole moment of the neighboring chains, even without including polarization. This means that better geometrical overlap of the backbones leads to a larger stabilization of holes. During the transition from a staggered to a coplanar stacking, the reduction in tilt angle leads to enhanced hole–quadrupole interactions. These are responsible for the lower $\langle U \rangle$ in CA-100 compared to CC-100. For the systems of lower regioregularity, the transition in backbone stacking is less pronounced because side-chain defects lead to a slight planarization of the backbone and, hence, lowered ionization potentials (compare the site-energy mean of CC-90 in Fig. 8 to that of CC-100). As the backbone stacking becomes entirely coplanar, side-chain defects lead to a high degree of slipping-type paracrystallinity. This implies a weakening of the energetically favorable hole–quadrupole interaction, and therefore an increase in the mean of the site-energy distribution when comparing CC-90 to CA-90. In addition to this shift of the mean, the slipping defects in CA-90 lead to a slight deviation from a Gaussian shape of the DOS.

Summing up, the external contribution to the energetic density of states in P3HT was shown to be intimately connected to paracrystallinity along the π -stacking direction, with the energetic disorder σ linearly related to the amplitude of backbone–backbone distance fluctuations, and the mean of the backbone–backbone distance distribution analogously related to the average site energy $\langle U \rangle$.

4.5 Charge Mobility

With the site energies and electronic couplings at hand, one can calculate charge transfer rates (see Sect. 4) for the set of electronically coupled pairs of conjugated segments. The directed graph that describes charge transport in the system is then fully parametrized and charge dynamics can be described via a master equation of the form:

$$\frac{\partial P_\alpha}{\partial t} = \sum_\beta [P_\beta K_{\beta \rightarrow \alpha} - P_\alpha K_{\alpha \rightarrow \beta}], \quad (36)$$

where P_α is the probability of finding the systems in state α . The rates $K_{\alpha \rightarrow \beta}$ are the transition rates from a state α to state β . For single-carrier dynamics, the number of available states α is the number of conjugated segments in the system, with each state associated with a molecule A being singly occupied. Using the single-site occupation probability p_A and transfer rates $k_{A \rightarrow B}$, Eq. (36) simplifies to:

$$\frac{\partial p_A}{\partial t} = \sum_B [p_B k_{B \rightarrow A} - p_A k_{A \rightarrow B}]. \quad (37)$$

This equation, valid in the limit of low charge densities, has the form $\partial_t \mathbf{p} = \tilde{\mathbf{k}} \mathbf{p}$ and can be solved using either linear solvers or a kinetic Monte Carlo (KMC) algorithm. A variable timestep size implementation of KMC is often used due to the broad distribution of rates $k_{A \rightarrow B}$, which easily spans many orders of magnitude.

The stationary solution of Eq. (37) can be used to evaluate a number of macroscopic observables. For comparison with TOF measurements, impedance spectroscopy, or similar, the charge-carrier mobility tensor $\tilde{\mu}$ at the electric field \mathbf{E} is calculated as:

$$\tilde{\mu} \mathbf{E} = \sum_{A,B} p_A k_{A \rightarrow B} (\mathbf{R}_A - \mathbf{R}_B). \quad (38)$$

Alternatively, when using KMC, the charge-carrier mobility along the direction of the external field \mathbf{E} can be obtained simply by:

$$\mu = \left\langle \frac{\Delta \mathbf{R} \cdot \mathbf{E}}{\Delta t |\mathbf{E}|^2} \right\rangle, \quad (39)$$

where $\langle \dots \rangle$ denotes averaging over all trajectories, Δt is the total run time of a trajectory, and $\Delta \mathbf{R}$ denotes the net displacement of the charge.

4.5.1 Charge-Carrier Mobility in P3HT Lamellae

Transport studies of different levels of complexity have been performed to study hole transport along the π -stacking direction of P3HT lamellae [13, 110]. Since the transport has a one-dimensional character, it can be anticipated that a broad and static distribution of electronic couplings (see also Sect. 4.6) limits charge mobility along lamellae [93, 111–117]. This is illustrated in Fig. 9, which shows that the mobility values, evaluated for 5,000 lamellae, each consisting of 40 stacked chains, are broadly distributed, with small mobilities as low as 10^{-7} cm²/V s.

It is important to relate the distribution of mobilities to those of electronic couplings and site energies. It has been found by comparing materials of different regioregularity that the associated mobility distributions are fundamentally different from those expected solely on the grounds of electronic couplings (see Fig. 7). The distribution of transfer integrals is determined by the polymorph at hand (*I'* or *I*) and not sensitive to a small decrease in regioregularity, whereas energetic disorder is governed by regioregularity defects and, as such, is polymorph-independent. Aiming for high mobilities, one should hence prefer high regioregularity over medium regioregularity due to the smaller energetic disorder, and prefer P3HT form *I'* over P3HT form *I* due to higher electronic couplings. The mobility implicitly depends on both quantities and as such mirrors a clear trend, with the average mobility decreasing in the order CC-100 > CA-100 > CC-90 > CA-90 [13]. These averages are indicated by vertical bars in Fig. 9. In the case of 100% regioregular P3HT, simulation results are in excellent agreement with field-effect mobilities in P3HT nanofibers (devoid of grain boundaries) extracted from experimental transistor I–V curves on P3HT nanofibers [14, 24, 118]. The range of experimental values ($\mu = 0.01$ – 0.06 cm²/V s) obtained for different solvent and processing conditions is shown as the gray bar in Fig. 9.

The effect of regioregularity on charge transport has been studied experimentally in the context of time-of-flight experiments [16], where a reduction in regioregularity by 5% led to a decrease in mobility by a factor of five. In simulations, a reduction in regioregularity by 10% translates into a factor of ten decrease in mobility, indicating that the decrease in mobility is due to intradomain instead of interdomain transport. According to [13], where the authors studied the intermolecular contribution to the DOS, the regioregularity effect is exclusively

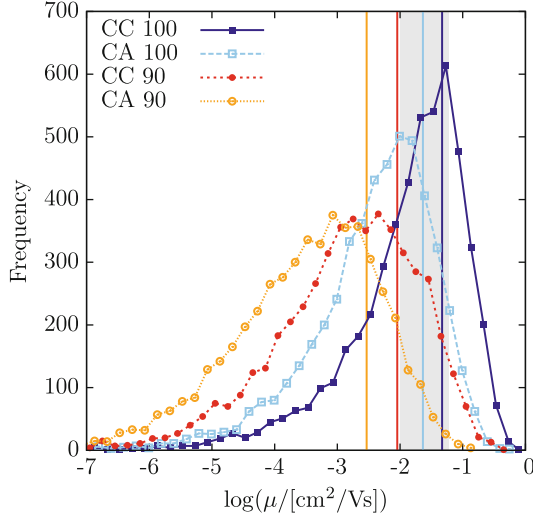


Fig. 9 Distributions of mobilities for CC-100, CA-100, CC-90, and CA-90. Vertical lines indicate averages. The gray bar includes the range of mobilities measured in P3HT nanofibers [14, 24, 118]. CA-100 corresponds to a system with a crystalline arrangement of backbones, amorphous packing of side-chains, and regioregularity of 100%. CC-100 corresponds to a system with crystalline side chains and 100% regioregularity. Adapted with permission from Poelking et al. [13]. Copyright (2013) American Chemical Society

due to increased energetic disorder. Additionally, the intramolecular contribution to the DOS was found to only have a negligible effect on localization length and, hence, transport in the high-regioregularity regime [108]. The conclusion is that the higher mobility in the more regioregular material is entirely attributable to a narrowing of the DOS that results from increased order in hole–quadrupole interaction distances.

The effect of energetic disorder is further amplified in the case of P3HT due to the one-dimensional character of transport, since a single energetic trap can impede transport through the entire lamella [93]. This effect is visualized in Fig. 10 [13], where the energetic landscape is exemplified for five different simulation times and four materials. Here, the widths of the bonds connecting the hopping sites are proportional to the logarithm of squared electronic coupling elements, while the heights of the vertical bars are proportional to the occupation probability of a specific site. The gray scale indicates the average mobility of a particular lamella, with darker colors corresponding to lower mobilities. One can see that site-energy profiles are highly corrugated and spatially correlated, with weaker correlations in the case of reduced regioregularity. Note also that the deep energetic traps found in CC-90 and CA-90 persist throughout the entire time range shown here, as expected from the associated time autocorrelation functions. Studying the landscape-mobility correlation more closely, it becomes apparent that transport in CC-100 and CA-100 is strongly dominated by weak links (small transfer integrals) that

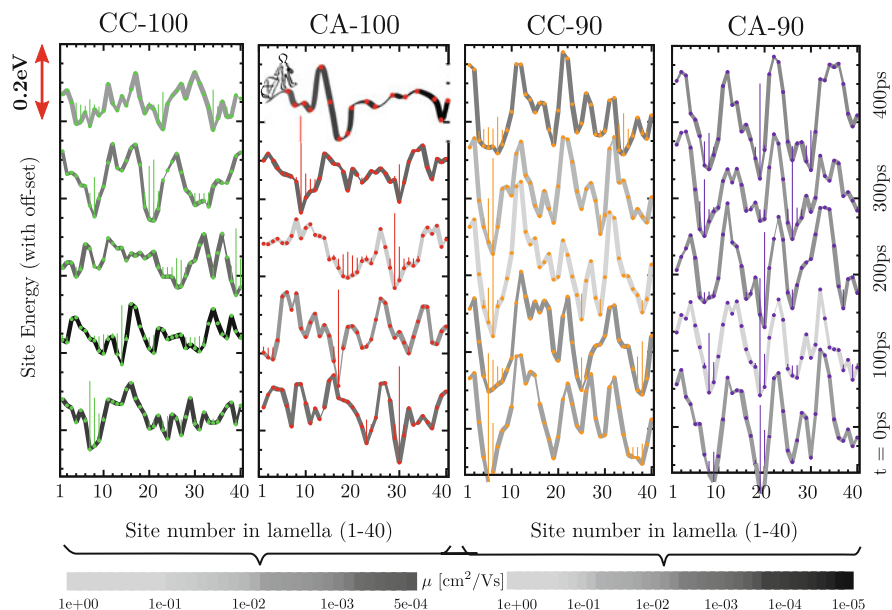


Fig. 10 The charge transport network for hole transport in polymeric lamellar crystals for five material systems from computer simulations: P3HT polymorphs CC (form I') and CA (form I), with regioregularities of 100 and 90%. Widths of *connecting lines* between neighboring sites and heights of *vertical lines* are proportional to the logarithm of squared transfer integrals and occupation probabilities, respectively. Mobilities are color-coded as indicated. Adapted with permission from Poelking et al. [13]. Copyright (2013) American Chemical Society

adversely affect the lamellar mobility, whereas transport in CC-90 and CA-90 suffers mostly from energetic disorder, as already suspected from the shape of the mobility distribution in Fig. 9.

To summarize, a small concentration of defects in side-chain attachment (90% regioregular P3HT) was shown to lead to a significant (factor of ten) decrease in charge-carrier mobility. This reduction is due to an increase in the intermolecular part of the energetic disorder and can be traced back to the amplified fluctuations in backbone-backbone distances, i.e., paracrystallinity.

4.6 Autocorrelation of Electronic Couplings and Site Energies

In the hopping picture, understanding the factors that limit charge-carrier mobility in polymers not only demands knowledge of the distribution of transport parameters, but also their time dependence. The latter is an important hint as to whether or not the hopping picture is justified to begin with, since there is no theoretical

technique currently available that can predict the regime of charge transport for a given material system. To explore the limitations associated with simulating charge transfer in a frozen morphology, Poelking et al. [13] have compared charge escape times τ_{esc} with relaxation times of the backbone, as reflected both in the electronic coupling elements and in site energies. The escape time (i.e., the average time a charge spends localized on a given site) is the inverse of the escape rate, $\tau_{\text{esc}}^{(i)} = 1/\Gamma_{\text{esc}}^{(i)}$, where $\Gamma_{\text{esc}}^{(i)} = \sum_{j(i)} \Gamma_{ij}$, Γ_{ij} is the hole-transfer rate from site i to site j , and the sum is evaluated for all nearest neighbors j of site i . From the resulting distribution of escape times, $p(t)$, one can calculate the distribution (exceedence, or complementary cumulative distribution function), $P(\tau) = \int_{\tau}^{\infty} p(t) dt$, which is proportional to the number of sites with an escape time larger than τ .

Backbone dynamics can be estimated from the time autocorrelation functions $R_U(\tau)$ for site energies $U^{(i)}$ and $R_J(\tau)$ for couplings $|J_{ij}|^2$:

$$R_U(\tau) = \frac{\langle (U_t^{(i)} - \langle U \rangle) (U_{t+\tau}^{(i)} - \langle U \rangle) \rangle}{\sigma^2}, \quad (40)$$

where the outer $\langle \dots \rangle$ denotes the ensemble average. The width σ and average $\langle U \rangle$ have the same meaning as in the electronic density of states (see Sect. 4.4). An analogous expression is used for the transfer integrals.

The autocorrelation function and the distribution of escape times for P3HT are summarized in Fig. 11. Relaxation of the electronic coupling elements and of the site energies occur on similar time scales in spite of their dissimilar physical origins: Site energies are related to long-range electrostatic interactions where averaging occurs over a large number of nearest neighbors and leads to spatial correlations. On the other hand, the electronic coupling elements (to a first approximation) only depend on the geometries of pairs of molecules, which results in increased sensitivity to thermal motion of the internal degrees of freedom. The reason for similar time scales is the chemical structure of P3HT: Every thiophene unit is linked to an alkyl side chain with slow dynamics both in the crystalline and amorphous phases. This overdamps the backbone dynamics, particularly torsional motions of thiophene units, and results in slow variations of electronic couplings. Interestingly, for the similar conjugated polymer PBTTT, where the thienothiophene unit is not linked to a side chain (implying a lower side-chain density and better crystallinity), the significantly faster dynamics of electronic couplings can boost the charge-carrier mobility [119].

Comparing the 100% and 90% regioregular materials, we can see how the defects in side-chain attachment lead to slower dynamics, with decorrelation times significantly increased over the defect-free case. More quantitatively, for intermediate delay times in the range of tenths of picoseconds, the time evolution is in all cases governed by a logarithmic diffusion-driven decorrelation of both site energies and electronic couplings. Regarding site energies, the dimensionless exponent that characterizes this decorrelation for CA-100 assumes a value three times larger than for CA-90. This again highlights how defects in regioregularity

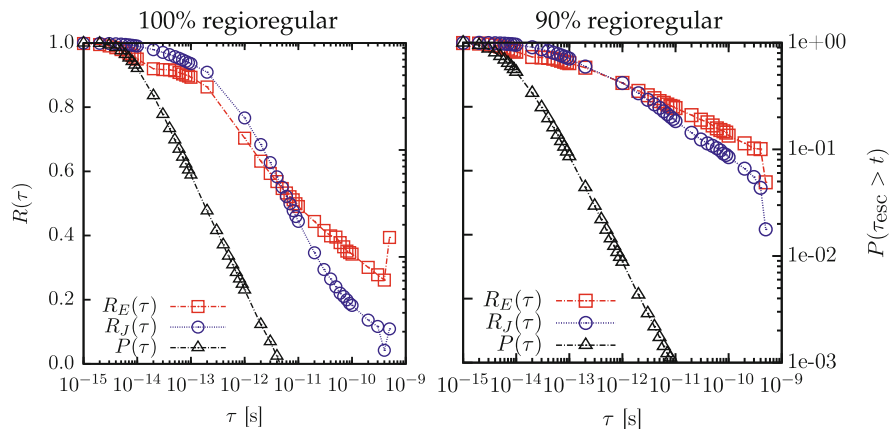


Fig. 11 The time scales of transport parameters in material systems of different regioregularity, estimated via the time autocorrelation function of transfer integrals (*blue circles*), site energies (*red squares*) and the tail distribution of escape times (*black triangles*). Adapted with permission from Poelking et al. [13]. Copyright (2013) American Chemical Society

induce glass-like features in structure and dynamics. Analyzing the de-correlation in polymorphs I' and I, this exponent remains the same. There is, however, an offset between the two time characteristics that persists up to delay times in the nanosecond range. This offset is a consequence of structural decorrelations within the first few femtoseconds: Side chains in form I are in a dynamically disordered state and, hence, damp backbone dynamics more effectively than the hexyl groups in form I'. This damping apparently dominates dynamics on this short time scale.

For P3HT, even the slowest escape times for holes do not extend into the decorrelation regime. Charge-carrier dynamics is therefore limited by the static disorder of electronic couplings and site energies, since their relaxation times exceed the typical time scales for hopping transport. Hence, it is possible to resort to a single charge-transfer rate to describe transport, Eq. (7), without time-averaging of electronic couplings of a pair of molecules, as needed for columnar discotic liquid crystals [120] or PBTTT [119].

5 First-Principles-Based Calculations for Large Models of Polymer

5.1 The Charge Localization–Length Problem

As we have seen in the previous sections, the definition of a reasonably accurate kinetic master equation from the microscopic structure can be achieved by combining atomistic simulations, quantum chemical calculations, and microelectrostatic

corrections. These methodologies require the definition of a ‘unit of transport’, i.e., a region of the polymer where the charge is assumed to reside. For transport in small molecules, liquid crystals, and some relatively short polymers it is straightforward to consider the full molecular unit as the unit of transport. It is also reasonable to consider long oligomers when studying transport in the direction perpendicular to the π - π stacking in semicrystalline phases. For amorphous regions in fully amorphous polymers, or if one is interested in the transport along the π -conjugated backbone, further approximations are needed. In the case of amorphous polymers like poly(*p*-phenylene vinylene) (PPV), the structure determined by classical simulations [121–123] contains regions where there is a strong deviation from planarity and it was proposed that the polymeric chain can be divided into conjugated portions defined as the regions between these conjugation-breaking distortions [124]. This idea has been used to interpret spectroscopic data but it is very difficult to apply it to computational systems. First of all, it is not clear how one can rigorously define a sharp threshold separating the complete conjugation breaking from the full conjugation between monomers. Moreover, there are many interesting polymers (including P3HT) that form crystalline domains so extended that no conjugation breaks are found for hundreds of nanometers [125]. The charge is certainly more localized than that, either by the disorder present in the semicrystalline phase or by electron–phonon coupling (evidence of charge localization can be found for example from charge-modulated spectroscopy [126, 127]). Determination of the localization characteristic of charge carriers in polymers is another important area of computational investigation that has been pursued by several groups over the past few years.

To determine the charge localization in a large system there is no other alternative than computing the electronic wavefunction of a large model system. The model systems are generated by classical simulation of polymers containing thousands of atoms, so it is not practical to study them in a charged state using quantum-mechanical methods. A calculation of the electronic structure of such a large model with an electron less than the neutral state would only yield the ground state, whereas one is generally interested in the energy distribution and localization of many charged states. The excited state of the charged simulation box cannot be computed with modern computational methods and therefore one cannot even evaluate the nuclear relaxation (reorganization energy) for the hopping between two states by starting with a large model system. For these reasons, all attempts to evaluate the wavefunction of a large model of polymers have focused on neutral systems and have interpreted the one-electron states (the orbitals) as the possible sites where the excess charge can be localized [107, 108]. Results are normally presented in terms of a density of states (DOS) and localization length but it should be noted that these two quantities are computed for systems with orbitals fully filled and empty above and below the band gap, respectively. Therefore, they cannot be directly compared with the models in Sect. 4, which include electron and nuclear polarization but have to make assumptions regarding the localization length.

For the one-electron states to be representative of the actual localization of the charge carrier, a further condition needs to be satisfied. The charge needs to be localized predominantly by the conformational disorder of the polymer and not by

the electron–phonon coupling. If this coupling is particularly strong, the frontier orbitals may be delocalized over many monomers. However, when an excess charge is added, the nuclear polarization localizes the charge, completely modifying the electronic wavefunction with respect to the neutral calculation. There is some general consensus [128, 129] that the localization of the wavefunction in P3HT largely originates from disorder and not from electron–phonon coupling because there is a correlation between increased order of P3HT and increased mobility [20]. Alternatively, one can be convinced that the conformational disorder is stronger than the electron–phonon coupling by comparing the polaron size of a perfectly ordered polymer chain with the localization of the orbitals computed from calculation of large realistic models of disordered chains. If the polaron size of the perfectly ordered system is much larger than the orbital in the disordered model, it is acceptable to determine the charge localization from calculations that neglect the electron–phonon coupling as a first approximation. Calculations for P3HT support this approximation [108, 130] but it should be noticed that polaron sizes are strongly dependent on the DFT methodology [131] and that the same assumption may not hold for the new families of semiconducting polymers [132], where large conjugated units are more weakly coupled by smaller conjugated linkers.

5.2 Strategies for Large-Scale Electronic-Structure Calculations of Polymer Models

Under the conditions that the calculation of a ground state wavefunction of a polymer model yields information about the charge localization for the carrier states, it is still not trivial to carry out such calculations. It is not obvious to know in advance how large a model of bulk polymer should be in order to reproduce the DOS and localization length without the results being affected by finite-size effects. The experience of available calculations with P3HT and PPV suggests that a model containing several chains of 20–40 monomers displays electronic properties that do not depend appreciably on the chain length [133] (it should not be forgotten that the morphology depends on the chain length up to much larger molecular weights [134]). Such models contain tens of thousands of atoms, a number that is still one order of magnitude larger than that normally achievable by current software specialized in linear scaling *ab initio* calculations, like SIESTA [135] or ONETEP [136]. It is certainly possible that such methods can be employed in the near future in benchmark calculations, but it is important to remember that what is needed is a methodology able to evaluate the wavefunction for many replicas of the equilibrated systems in order to provide statistically meaningful results.

However, ideas from linear scaling methodologies can be used to develop *ad hoc* methods that are able to compute in a more approximate fashion the wavefunction for large systems. Essentially, all linear scaling methods are based on the definition of a very localized basis set that reduces the number of matrix elements to be

evaluated to a value that scales linearly with the size of the system [135–137]. For organic polymers, it seems natural to describe the polymer orbitals as a linear combination of monomer orbitals. It is possible to reduce the number of orbitals per monomer to be considered (e.g., from HOMO-1 to LUMO+1 in P3HT), thus reducing the size of the one-electron effective Hamiltonian. Different schemes have been proposed for evaluating the diagonal and off-diagonal elements of such a reduced Hamiltonian, including a fragment molecular orbital approach [138] and a charge patching method [107, 139, 140]. Their calculation of the matrix elements shares many points with the methodology described in Sect. 4.3, except that the calculations are always performed for the neutral state. A general formalism for such methods has been developed by the quantum chemistry community [137, 141–143] and has the obvious advantage of being very intuitive: All matrix elements entering in the Hamiltonian have a clear physical meaning.

The various partitioning schemes proposed for polymer systems are very often complemented by further approximations that take into account the chemical structure of the investigated system. As the frontier orbitals are invariably localized on the conjugated fragment of the monomer, while a large fraction of the molecular weight is taken up by the polymer side chains that do not contribute to the charge transport states, it is customary to remove the side chains from the calculation, sometimes substituting them with effective point charges that simulate the missing electrostatic effects [133]. For lamellar systems such as P3HT and PBTTT, it is an excellent approximation to neglect completely the electronic coupling between lamellae, therefore describing a system that is essentially two-dimensional [108, 144].

A relatively simple approach that can be considered the simplest possible Hamiltonian partitioning technique has been proposed recently for the calculation of the electronic properties of MEH-PPV [133]. Here the amorphous-polymer model is simply partitioned into subsystems containing single chains (surrounded by point charges reproducing the local electrostatic potential and with shortened side chains). The full wavefunction of each single chain can be computed with routine DFT calculations and the electronic couplings between chains can be evaluated similarly. The coupling between polymer orbitals localized on different chains is very small because only a few atoms localized on different chains are in contact while the orbitals are typically localized over several monomers. A further reduction in computational cost can be achieved using a small basis set, which, at least for this type of polymer, does not seem to affect the shape of the DOS or the localization length.

An alternative approach to full or ad hoc linear scaling DFT methods is calculation through approximate DFT methods such as the tight binding DFT (DFTB) [145]. This family of methods has been developed over the past few years and the most convenient version of the methodology is the self-consistent charge-density functional tight binding (SCC-DFTB) [146], as implemented for example in the software DFTB+. An acceleration of one to two orders of magnitudes for the electronic structure calculation is achieved by an approximate evaluation of the Kohn–Sham–Fock matrix elements in the atomic-orbital basis. A very broad range

of applications apart from organic semiconductors have been proposed [143], but relatively few results have been reported for semiconducting polymers [147] even though great success has been achieved in the study of charge transfer processes in biophysical systems [148, 149], which provide a similar level of computational challenge.

Finally, an obvious choice for calculation of the large-scale electronic structure would be via semi-empirical methods. These have been the methods of choice for many years for exploring charge [150] and exciton [151] dynamics in single-chain polymers containing only carbon and hydrogen (e.g., PPV, polyethylene). However, there are very few systematic studies of their reliability for polymers containing heteroatoms such as S, F, Se, and Ge, which are featured in a large number of new polymers.

Although there seems to be no lack of options for the calculation of the wavefunction of large models of polymeric systems, these calculations have been attempted on a very limited number of systems. One of the main objectives of future computational studies is to perform calibration of these methodologies, whereby the results obtained with different approximate electronic structure methods on the same structural models are compared.

5.3 Results from the Computation of the Wavefunction for Large-Scale Polymer Models

The calculations performed on models of polymers, according to any of the methodologies described in the previous section, provide in the first instance the DOS and a measure of the localization length of the states relevant for transport, i.e., those located at the edge of the valence (or conduction) band for holes (or electrons). For all polymers considered (amorphous and semicrystalline), the states deep in the tail of the DOS are more localized and the localization length increases as states deeper in the band are considered (see Fig. 12), as predicted by simplified generic polymer models [152]. The chemical description of these states in the tail is potentially very useful because it may suggest possible routes for increasing the charge mobility by reducing the number of trap states.

Calculations suggest that hole trap states (high-energy occupied orbitals) are found in regions of P3HT where the conjugated backbone is more planar than on average [108, 153]. The possibility of different degrees of planarity generates regions where the HOMO–LUMO gap is smaller, coinciding with the more planar segments of P3HT. Not surprisingly, when regioregularity defects are introduced, the trap states become localized far away from the regioregularity defect and, for this reason, the total number of trap states is not much affected by the regioregularity. This has also been found experimentally [108].

By adopting fast methods for calculation of the electronic structure, it is possible to monitor the lifetime of these trap states by repeating the electronic structure

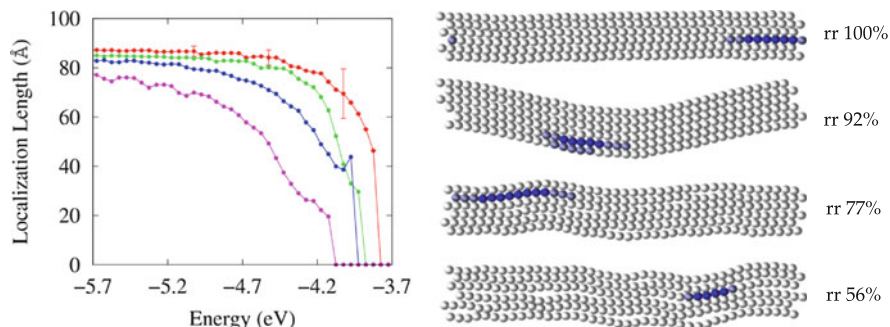


Fig. 12 *Left*: Average localization length in an ordered region of P3HT with regioregularities of 56% (magenta, lowest curve), 77% (blue), 92% (green) and 100% (red, uppermost curve). The error bars of a few selected points are larger in the tail region, indicating the coexistence of localized and delocalized states in that region. *Right*: Localization of the orbital density for the state at the band edge (dark blue regions correspond to higher density) on each P3HT monomer (represented as a sphere) for different polymer regioregularities. Adapted with permission from McMahon et al. [108]. Copyright (2013) American Chemical Society

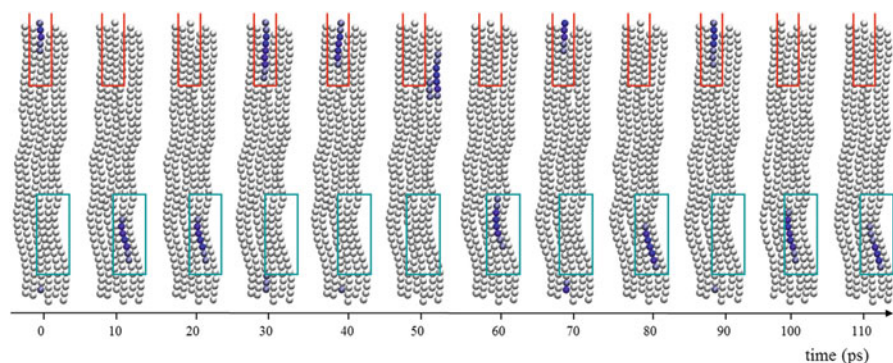


Fig. 13 Localization of the HOMO orbital density on each monomer in a P3HT lamella with low regioregularity during part of the molecular dynamics trajectory. The orbital density (dark regions correspond to higher density) is localized (except at 50 ps) in one of the two regions indicated by rectangles. Adapted with permission from McMahon et al. [108]. Copyright (2013) American Chemical Society

calculation for different snapshots obtained via classical molecular dynamics (see Fig. 13). For P3HT, the most stable trap states are stable for many tens of picoseconds, i.e., it is possible to think that these trap states are static defects from the point of view of the moving charge carrier [153]. Further analysis shows that these local deformations within the semicrystalline domain are stabilized by gauche conformations in the side chain. A similar analysis on PBTTT shows instead that the trap states appear and disappear in different parts of the chain within a few tens of picoseconds, i.e., there are no long-lived trap states in PBTTT

[147]. Considering that it was not possible to find a clear correlation between the geometry of the chain and the existence of trap states, it was argued that the excellent charge mobility in PBTTT could be due to the limited number of trap states that are supported by the PBTTT morphology.

The attempt to correlate the local structure of the polymer with the localization of the orbitals also yielded some interesting and counterintuitive results [133]. In amorphous PPV, a significant number of high-energy occupied orbitals was found in highly bent regions of the polymer spanning two fragments that, by considering the shape of the polymer, ought to be considered belonging to two separate conjugated units. Considering all the available studies together, it seems that simple intuitive arguments are not sufficient to qualitatively predict the relation between the local geometric structure of a polymer and the localization of its orbitals.

Once the one-electron states of a large system have been evaluated, it is very challenging to derive a fully satisfactory master equation like Eq. (36) that describes the hopping rate between these approximate states. Vukmirović and Wang have proposed a perturbative expression assuming that these states are coupled by nonadiabatic coupling terms that can be evaluated explicitly [107] or can be approximated using the overlap between the absolute value of the wavefunction [154]. Remarkably, the proposed expression does not contain the effect of nuclear polarization in the presence of an additional charge (reorganization energy) and so it is strictly valid in the limit of vanishing reorganization energy like Miller–Abrahams rates [155]. Using this approach it was highlighted that the DOS does not contain all the information needed to evaluate the mobility and that it is possible to have reduced broadening of the DOS due to increased order, but still have low mobility because the coupling between states is reduced [156]. Alternative methods for combining nuclear polarization and disorder effects have been proposed but they have so far only been applied to highly simplified model systems [157, 158].

Ideally, such large-scale calculations should be able to incorporate the effect of nuclear and electronic polarization but, as outlined in Sect. 5.2, it is not clear how such generalizations could be introduced within the available methodologies.

6 Outlook

To conclude, substantial method development is still required in order to achieve parameter-free modeling of organic semiconductors. Imperative for predicting large-scale morphologies are accurate polarizable force fields and computationally efficient coarse-grained models. These models should be capable of describing backbone crystallization and allow for reintroduction of atomistic details. Essential for charge transport are extensions of large-scale, first-principles methods to charged states. Challenges are the incorporation of polaronic effects and a unified description of charge transfer along a single chain and between conjugated segments located on different chains. Last but not least, molecular charge transfer

parameters must be included into a hybrid kinetic Monte–Carlo scheme, with transfer rates updated on the fly to account for long-range electrostatic and polarization effects.

Acknowledgments This work was partly supported by the DFG program IRTG 1404, DFG grant SPP 1355, and BMBF grants MEDOS (FKZ 03EK3503B), MESOMERIE (FKZ 13N10723), and MORPHEUS (FKZ 13N11704). We thank Patrick Gemünden for fruitful collaborations and discussions. We are grateful to Jeroen van der Holst, Mara Jochum and Kurt Kremer for critical reading of the manuscript.

References

1. McCullough RD (1998) *Adv Mater* 10(2):93–116
2. McCullough RD, Lowe RD (1992) *Chem Commun* 1992(1):70
3. Meyer V (1883) *Berichte der deutschen chemischen Gesellschaft* 16(1):1465
4. Yamamoto T, Sanechika K, Yamamoto A (1980) *J Polym Sci Polym Lett Ed* 18(1):9
5. Lin JWP, Dudek LP (1980) *J Polym Sci Polym Chem Ed* 18(9):2869
6. Elsenbaumer R, Jen K, Oboodi R (1986) *Synth Met* 15(2–3):169
7. Perepichka IF, Perepichka DF, Meng H (2009) Thiophene-based materials for electroluminescent applications. In: Perepichka IF, Perepichka DF (ed), *Handbook of thiophene-based materials*. Wiley, Hoboken, p 695–756
8. Prosa TJ, Winokur MJ, McCullough RD (1996) *Macromolecules* 29(10):3654
9. Brinkmann M (2011) *J Polym Sci B Polym Phys* 49(17):1218
10. Wu Z, Petzold A, Henze T, Thurn-Albrecht T, Lohwasser RH, Sommer M, Thelakkat M (2010) *Macromolecules* 43(10):4646
11. Yuan Y, Zhang J, Sun J, Hu J, Zhang T, Duan Y (2011) *Macromolecules* 44(23):9341
12. Dudenko D, Kiersnowski A, Shu J, Pisula W, Sebastiani D, Spiess HW, Hansen MR (2012) *Angew Chem Int Ed* 51(44):11068
13. Poelking C, Andrienko D (2013) *Macromolecules* 46(22):8941
14. Shimomura T, Takahashi T, Ichimura Y, Nakagawa S, Noguchi K, Heike S, Hashizume T (2011) *Phys Rev B* 83(11):115314
15. Li G, Shrotriya V, Huang J, Yao Y, Moriarty T, Emery K, Yang Y (2005) *Nat Mater* 4(11):864
16. Mauer R, Kastler M, Laquai F (2010) *Adv Funct Mater* 20(13):2085
17. Ballantyne AM, Chen L, Dane J, Hammant T, Braun FM, Heeney M, Duffy W, McCulloch I, Bradley DDC, Nelson J (2008) *Adv Funct Mater* 18(16):2373–2380
18. Tsumura A, Koezuka H, Ando T (1986) *Appl Phys Lett* 49(18):1210
19. Bao Z, Dodabalapur A, Lovinger AJ (1996) *Appl Phys Lett* 69(26):4108
20. Chang JF, Clark J, Zhao N, Sirringhaus H, Breiby DW, An-dreasen JW, Nielsen MM, Giles M, Heeney M, McCulloch I (2006) *Phys Rev B* 74(11):115318
21. Kline RJ, McGehee MD, Kadnikova EN, Liu J, Fréchet JMJ, Toney MF (2005) *Macromolecules* 38(8):3312
22. Zen A, Paum J, Hirschmann S, Zhuang W, Jaiser F, Asawapirom U, Rabe JP, Scherf U, Neher D (2004) *Adv Funct Mater* 14(8):757–764
23. Merlo JA, Frisbie CD (2003) *J Polym Sci B Polym Phys* 41(21):2674–2680
24. Bolsée JC, Oosterbaan WD, Lutsen L, Vanderzande D, Manca J (2011) *Org Electron* 12(12):2084
25. Raos G, Famulari A, Marcon V (2003) *Chem Phys Lett* 379(3–4):364
26. Darling SB, Sternberg M (2009) *J Phys Chem B* 113(18):6215, PMID: 19290596
27. Marchiori C, Koehler M (2010) *Synth Met* 160(7–8):643

28. Bhatta RS, Yimer YY, Tsige M, Perry DS (2012) *Comput Theor Chem* 995:36
29. Tsuzuki S, Honda K, Azumi R (2002) *J Am Chem Soc* 124(41):12200
30. Bhatta RS, Perry DS (2013) *Comput Theor Chem* 1008:90
31. Baggioli A, Famulari A (2014) *Phys Chem Chem Phys* 16:3983-3994
32. Maillard A, Rochefort A (2009) *Phys Rev B* 79(11):115207
33. Colle R, Grosso G, Ronzani A, Zicovich-Wilson CM (2011) *Physica Status Solidi B* 248(6):1360-1368
34. Xie W, Sun YY, Zhang SB, Northrup JE (2011) *Phys Rev B* 83(18):184117
35. Famulari A, Raos G, Baggioli A, Casalegno M, Po R, Meille SV (2012) *J Phys Chem B* 116(49):14504
36. Dag S, Wang LW (2010) *J Phys Chem B* 114(18):5997
37. Marcon V, Raos G (2004) *J Phys Chem B* 108(46):18053
38. Moreno M, Casalegno M, Raos G, Meille SV, Po R (2010) *J Phys Chem B* 114(4):1591
39. To TT, Adams S (2012) *Nanosci Nanotechnol Lett* 4(7):703
40. Bhatta RS, Yimer YY, Perry DS, Tsige M (2013) *J Phys Chem B* 117(34):10035
41. Melis C, Colombo L, Mattoni A (2011) *J Phys Chem C* 115(2):576
42. Alexiadis O, Mavrantzas VG (2013) *Macromolecules* 46(6):2450
43. Curcó D, Alemán C (2007) *J Comput Chem* 28(10):1743-1749
44. Zhang G, Pei Y, Ma J, Yin K, Chen CL (2004) *J Phys Chem B* 108(22):6988
45. Huang DM, Faller R, Do K, Moulé AJ (2010) *J Chem Theory Comput* 6(2):526
46. Do K, Huang DM, Faller R, Moulé AJ (2010) *Phys Chem Chem Phys* 12(44):14735
47. Yimer YY, Dhinojwala A, Tsige M (2012) *J Chem Phys* 137(4):044703
48. Reddy S, Kuppa VK (2012) *Synth Met* 162(23):2117
49. D'Avino G, Mothy S, Muccioli L, Zannoni C, Wang L, Cornil J, Beljonne D, Castet F (2013) *J Phys Chem C* 117(25):12981
50. Lee CK, Pao CW, Chu CW (2011) *Energ Environ Sci* 4(10):4124
51. Müller M (2011) *J Stat Phys* 145(4):967
52. Noid WG (2013) *J Chem Phys* 139(9):090901
53. Kremer K, Müller-Plathe F (2002) *Mol Simulat* 28(8-9):729
54. Lyubartsev AP, Laaksonen A (1995) *Phys Rev E* 52(4):3730
55. Izvekov S, Voth GA (2005) *J Phys Chem B* 109(7):2469
56. Noid WG, Chu J, Ayton GS, Krishna V, Izvekov S, Voth GA, Das A, Andersen HC (2008) *J Chem Phys* 128:244114
57. Shell MS (2008) *J Chem Phys* 129(14):144108
58. Daoulas KC, Müller M (2010) Comparison of simulations of lipid membranes with membranes of block copolymers. In: Meier WP, Knoll W (eds) *Polymer membranes/biomembranes. Advances in Polymer Science*, vol 224. Springer, Berlin Heidelberg, pp 43-85
59. Jankowski E, Marsh HS, Jayaraman A (2013) *Macromolecules* 46(14):5775
60. Schwarz KN, Kee TW, Huang DM (2013) *Nanoscale* 5(5):2017
61. Reith D, Pütz M, Müller-Plathe F (2003) *J Comput Chem* 24(13):1624-1636
62. Carbone P, Varzaneh HAK, Chen X, Müller-Plathe F (2008) *J Chem Phys* 128(6):064904
63. Daoulas KC, Rühle V, Kremer K (2012) *J Phys Condens Mat* 24(28):284121
64. Gemünden P, Poelking C, Kremer K, Andrienko D, Daoulas KC (2013) *Macromolecules* 46(14):5762
65. Stingelin N (2012) *Polym Int* 61(6):866-873
66. Ho V, Boudouris BW, Segalman RA (2010) *Macromolecules* 43(19):7895
67. Holyst R, Vilgis TA (1996) *Macromol Theor Simulat* 5(4):573-643
68. Hamm M, Goldbeck-Wood G, Zvelindovsky AV, Sevink GJA, Fraaije JGEM (2002) *J Chem Phys* 116(7):3152
69. Wang Q (2011) *Soft Matter* 7(8):3711
70. Pryamitsyn V, Ganesan V (2004) *J Chem Phys* 120(12):5824
71. Kumar NA, Ganesan V (2012) *J Chem Phys* 136(10):101101

72. Vettorel T, Besold G, Kremer K (2010) *Soft Matter* 6(10):2282
73. Helfand E, Tagami Y (2003) *J Chem Phys* 56(7):3592
74. Daoulas KC, Müller M (2006) *J Chem Phys* 125(18):184904
75. Detcheverry FA, Pike DQ, Nealey PF, Müller M, Pablo JJD (2009) *Faraday Discuss* 144:111
76. Kron AK (1965) *Polym Sci USSR* 7(7):1361
77. Wall FT, Mandel F (2008) *J Chem Phys* 63(11):4592
78. Rühle V, Kirkpatrick J, Andrienko D (2010) *J Chem Phys* 132(13):134103
79. Marcus RA (1993) *Rev Mod Phys* 65(3):599
80. May V, Kühn O (2011) *Charge and energy transfer dynamics in molecular systems*, 3rd edn. Wiley-VCH, Weinheim
81. Grabert H, Weiss U (1985) *Phys Rev Lett* 54(15):1605
82. Fisher MPA, Dorsey AT (1985) *Phys Rev Lett* 54(15):1609
83. Rühle V, Lukyanov A, May F, Schrader M, Vehoff T, Kirkpatrick J, Baumeier B, Andrienko D (2011) *J Chem Theory Comput* 7(10):3335
84. Asadi K, Kronemeijer AJ, Cramer T, Jan Anton Koster L, Blom PWM, de Leeuw DM (2013) *Nat Commun* 4:1710
85. Reimers JR (2001) *J Chem Phys* 115(20):9103
86. Hsu CP (2009) *Accounts Chem Res* 42(4):509
87. Valeev EF, Coropceanu V, da Silva Filho DA, Salman S, Brédas JL (2006) *J Am Chem Soc* 128(30):9882
88. Brédas JL, Calbert JP, Filho DADS, Cornil J (2002) *Proc Natl Acad Sci USA* 99(9):5804
89. Coropceanu V, Cornil J, da Silva Filho DA, Olivier Y, Silbey R, Brédas JL (2007) *Chem Rev* 107(4):926
90. Kirkpatrick J (2008) *Int J Quantum Chem* 108(1):51, Bibtext: Kirkpatrick 2008
91. Baumeier B, Kirkpatrick J, Andrienko D (2010) *Phys Chem Chem Phys* 12(36):11103
92. Fogel Y, Zhi L, Rouhanipour A, Andrienko D, Räder HJ, Müllen K (2009) *Macromolecules* 42(18):6878
93. Scher H, Alexander S, Montroll EW (1980) *Proc Natl Acad Sci U S A* 77(7):3758
94. Stone AJ (1997) *The theory of intermolecular forces*. Clarendon, Oxford
95. Hättig C (1996) *Chem Phys Lett* 260(3–4):341
96. Hättig C, Heß BA (1994) *Mol Phys* 81(4):813
97. Verstraelen T, Pauwels E, De Proft F, Van Speybroeck V, Geerlings P, Waroquier M (2012) *J Chem Theory Comput* 8(2):661
98. Breneman CM, Wiberg KB (1990) *J Comput Chem* 11(3):361–373
99. Stone A, Alderton M (1985) *Mol Phys* 56(5):1047
100. Stone AJ (2005) *J Chem Theory Comput* 1(6):1128
101. Kramer C, Bereau T, Spinn A, Liedl KR, Gedeck P, Meuwly M (2013) *J Chem Inf Model* 53(12):3410
102. Chirlan LE, Francl MM (1987) *J Comput Chem* 8(6):894
103. Thole B (1981) *Chem Phys* 59(3):341
104. van Duijnen PT, Swart M (1998) *J Phys Chem A* 102(14):2399
105. Applequist J, Carl JR, Fung KK (1972) *J Am Chem Soc* 94(9):2952
106. Ren P, Ponder JW (2003) *J Phys Chem B* 107(24):5933
107. Vukmirović N, Wang LW (2011) *J Phys Chem B* 115(8):1792
108. McMahon DP, Cheung DL, Goris L, Dacuna J, Salleo A, Troisi A (2011) *J Phys Chem C* 115(39):19386
109. Baessler H (1993) *Phys Status Solidi B* 175(1):15
110. Lan YK, Yang CH, Yang HC (2010) *Polym Int* 59(1):16
111. Kirkpatrick J, Marcon V, Nelson J, Kremer K, Andrienko D (2007) *Phys Rev Lett* 98(22):227402
112. Marcon V, Kirkpatrick J, Pisula W, Andrienko D (2008) *Phys Status Solidi B* 245(5):820–824

113. Andrienko D, Kirkpatrick J, Marcon V, Nelson J, Kremer K (2008) *Phys Status Solidi B* 245 (5):830
114. Nelson J, Kwiatkowski JJ, Kirkpatrick J, Frost JM (2009) *Accounts Chem Res* 42(11):1768
115. May F, Marcon V, Hansen MR, Grozema F, Andrienko D (2011) *J Mater Chem* 21(26):9538
116. Schrader M, Fitzner R, Hein M, Elschner C, Baumeier B, Leo K, Riede M, Bäuerle P, Andrienko D (2012) *J Am Chem Soc* 134(13):6052
117. Schrader M, Körner C, Elschner C, Andrienko D (2012) *J Mater Chem* 22(41):22258
118. Mas-Torrent M, Boer DD, Durkut M, Hadley P, Schenning APHJ (2004) *Nanotechnology* 15 (4):S265
119. Poelking C, Ivanov V, Kremer K, Risko C, Brédas JL, Andrienko D, Eunkyung C (2013) *J Phys Chem C* 117(4):1633
120. Olivier Y, Muccioli L, Lemaire V, Geerts YH, Zannoni C, Cornil J (2009) *J Phys Chem B* 113 (43):14102
121. De Leener C, Hennebicq E, Sancho-Garcia JC, Beljonne D (2009) *J Phys Chem B* 113 (5):1311
122. DuBay KH, Hall ML, Hughes TF, Wu C, Reichman DR, Friesner RA (2012) *J Chem Theory Comput* 8(11):4556
123. Kumar P, Mehta A, Mahurin SM, Dai S, Dadmun MD, Sumpter BG, Barnes MD (2004) *Macromolecules* 37(16):6132
124. Collini E, Scholes GD (2009) *Science* 323(5912):369, PMID: 19150843
125. Salleo A, Kline RJ, DeLongchamp DM, Chabinyc ML (2010) *Adv Mater* 22(34):3812–3838
126. Beljonne D, Cornil J, Sirringhaus H, Brown PJ, Shkunov M, Friend RH, Brédas JL (2001) *Adv Funct Mater* 11(3):229–234
127. Brown PJ, Sirringhaus H, Harrison M, Shkunov M, Friend RH (2001) *Phys Rev B* 63 (12):125204
128. Magin EH, Borsenberger PM (1993) *J Appl Phys* 73(2):787
129. Van der Auweraer M, De Schryver FC, Borsenberger PM, Bässler H (1994) *Adv Mater* 6 (3):199–213
130. Zade SS, Zamoshchik N, Bendikov M (2011) *Accounts Chem Res* 44(1):14
131. Nayyar IH, Batista ER, Tretiak S, Saxena A, Smith DL, Martin RL (2013) *J Chem Theory Comput* 9(2):1144
132. Bronstein H, Chen Z, Ashraf RS, Zhang W, Du J, Durrant JR, Shakya Tuladhar P, Song K, Watkins SE, Geenen Y, Wienk MM, Janssen RAJ, Anthopoulos T, Sirringhaus H, Heeney M, McCulloch I (2011) *J Am Chem Soc* 133(10):3272
133. Qin T, Troisi A (2013) *J Am Chem Soc* 135(30):11247
134. Shaked S, Tal S, Roichman Y, Razin A, Xiao S, Eichen Y, Tessler N (2003) *Adv Mater* 15 (11):913–916
135. Soler JM, Artacho E, Gale JD, García A, Junquera J, Ordejón P, Sánchez-Portal D (2002) *J Phys Condens Mat* 14(11):2745
136. Skylaris CK, Haynes PD, Mostofi AA, Payne MC (2005) *J Chem Phys* 122(8):084119
137. Gordon MS, Mullin JM, Pruitt SR, Roskop LB, Slipchenko LV, Boatz JA (2009) *J Phys Chem B* 113(29):9646
138. McMahon DP, Troisi A (2009) *Chem Phys Lett* 480(4–6):210
139. Vukmirović N, Wang LW (2009) *J Phys Chem B* 113(2):409
140. Vukmirović N, Wang LW (2009) *Nano Lett* 9(12):3996
141. Fedorov DG, Kitaura K (2007) *J Phys Chem A* 111(30):6904
142. Kitaura K, Ikeo E, Asada T, Nakano T, Uebayasi M (1999) *Chem Phys Lett* 313(3–4):701
143. Kubař T, Elstner M (2013) *J R Soc Interface* 10(87):20130415, PMID: 23883952
144. Liu J, Sun Y, Gao X, Xing R, Zheng L, Wu S, Geng Y, Han Y (2011) *Langmuir* 27(7):4212
145. Porezag D, Frauenheim T, Köhler T, Seifert G, Kaschner R (1995) *Phys Rev B* 51(19):12947
146. Elstner M, Porezag D, Jungnickel G, Elsner J, Haugk M, Frauenheim T, Suhai S, Seifert G (1998) *Phys Rev B* 58(11):7260
147. Liu T, Troisi A (2014) *Adv Funct Mater* 24(7):925–933

148. Kubař T, Elstner M (2010) *J Phys Chem B* 114(34):11221
149. Kubař T, Kleinekathöfer U, Elstner M (2009) *J Phys Chem B* 113(39):13107
150. Johansson Å, Stafström S (2001) *Phys Rev Lett* 86(16):3602
151. Barford W, Trembath D (2009) *Phys Rev B* 80(16):165418
152. Noriega R, Rivnay J, Vandewal K, Koch FPV, Stingelin N, Smith P, Toney MF, Salleo A (2013) *Nat Mater* 12(11):1038
153. Cheung DL, McMahon DP, Troisi A (2009) *J Am Chem Soc* 131(31):11179
154. Vukmirović N, Wang LW (2010) *Appl Phys Lett* 97(4):043305
155. Miller A, Abrahams E (1960) *Phys Rev* 120(3):745
156. Vukmirović N (2013) *Phys Chem Chem Phys* 15(10):3543
157. Bronold FX, Alvermann A, Fehske H (2004) *Phil Mag* 84(7):673
158. Fornari RP, Troisi A (2014) *Phys Chem Chem Phys* 16(21):9997